https://doi.org/10.5194/acp-2019-502
Preprint. Discussion started: 21 June 2019
© Author(s) 2019. CC BY 4.0 License.

Atmospheric Chemistry and Physics Discussions

Statistical Analysis of Ice Microphysical Properties in Tropical Mesoscale Convective Systems Derived from Cloud Radar and In-Situ Microphysical Observations

Emmanuel Fontaine[1,6*], Alfons Schwarzenboeck[1], Delphine Leroy[1], Julien Delanoë[2], Alain Protat[3], Fabien Dezitter[4], John Walter Strapp[5], Lyle Edward Lilie[5].

[1]Laboratoire de Météorologie Physique, UCA, CNRS, Aubière, France
[2]Laboratoire Atmosphère, Milieux et Observations Spatiales, UVSQ, Guyancourt, France
[3]Center for Australian Weather and Climate Research, Melbourne, Australia
[4]Airbus Helicopters, Toulouse, France
[5]Met Analytics, Toronto, Canada
[6*]now at Department of Atmospheric Sciences, National Taiwan University, Taipei, Taiwan

Correspondence to: E. Fontaine (emmanuel.r.j.fontaine@gmail.com)

Abstract. This study presents a statistical analysis of the properties of ice hydrometeors in tropical mesoscale convective systems observed during four different aircraft campaigns. Among the instruments on board the aircraft, we focus on the synergy of a 94GHz cloud radar and 2 optical array probes (OAP; measuring hydrometeor sizes from 10µm to about 1cm). For two campaigns, an accurate simultaneous measurement of the ice water content is available, while for the two others, ice water content is retrieved from the synergy of the radar reflectivity measurements and hydrometeor size and morphological retrievals from OAP probes. The statistics of ice hydrometeor properties is calculated as a function of radar reflectivity factor measurement percentiles and temperature. Hence, mesoscale convective systems (MCS) microphysical properties (ice water content, visible extinction, mass-size relationship coefficients, total concentrations and second and third moment of hydrometeors size distribution) are sorted in temperature (thus altitude) zones, and subsequently each individual campaign is analysed with respect to median microphysical properties of the global dataset (merging all 4 campaign datasets). The study demonstrates that ice water content (IWC), visible extinction, total crystal concentration, and second and third moments of hydrometeors size distributions are similar in all 4 type of MCS for IWC larger than 0.1g m^{-3}. Finally, two parameterizations are developed for deep convective systems. The first one concerns the calculation of the visible extinction as a function of temperature and ice water content. The second one concerns the calculation of hydrometeor size distributions as a function of ice water content and temperature that can be used in numerical weather prediction.

1 Introduction

Defining clouds and how they interact with the atmosphere is a major challenge in climate sciences and meteorology. Clouds play an important role in the evolution of ~~the~~ weather and climate on the Earth. They affect the dynamics and the thermodynamics of the troposphere, and impact the radiative transfer of energy in thermal and visible wavelengths by heating or cooling the atmosphere. In addition, clouds represent an important part of the hydrological cycle, due to evaporation and precipitation processes. Inversely, dynamic features such as the Madden Julian oscillation (MJO, perturbation of large scale circulation leading to an eastward propagation of organized convective activity) can also affect the development of deep convective clouds (Madden and Julian, 1994, 1971). Mesoscale Convective Systems (MCS) are complex clouds and are the result of specific synoptic conditions and mesoscale instabilities which lead to the development of cumulonimbus (Houze, 2004). The complexity of MCS is also relying on the dynamical, radiative, and precipitation characteristics which depend on the location in the evolving MCS (Houze, 2004). MCS can last several hours and can affect human societies in different ways. Indeed, MCS are often associated with hazardous weather events such as landslides, flash floods, aircraft incidents, and tornadoes, all which can cause loss of human lives.

https://doi.org/10.5194/acp-2019-502
Preprint. Discussion started: 21 June 2019
© Author(s) 2019. CC BY 4.0 License.

Atmospheric Chemistry and Physics Discussions

Weather and climate models use rather simplified schemes to describe the ice hydrometeors properties. Parametrization disagreements due to larger uncertainties in the representation of ice properties in clouds (Li et al., 2007, 2005) lead to large variations in the quantification of ice cloud effects on climate evolution (Intergovernmental Panel on Climate Change Fourth Assessment Report). An accurate estimation of the spatiotemporal distribution of the Ice Water Content (IWC) is a key parameter for evaluating and improving numerical weather prediction (Stephens et al., 2002). Underlying hydrometeor growth processes in MCS vary in time (growing, maturing, decaying phase) but also in space, in other words horizontally (distance from active convective zone) and vertically (as function of temperature).

A number of studies (Gayet et al. (2012); Lawson et al. (2010) and Stith et al. (2014)), demonstrate a large variability of ice hydrometeors present in evolving MCS. In the active convective area, large super cooled droplets were observed near -4°C and rimed ice hydrometeors below -11°C. Also at -47°C large rimed particles from updraft regions coexisting with small ice crystals (pristine ice) were encountered. Near the convective zone of MCS (i.e fresh anvil) presence of pristine ice, aggregates of hexagonal plates and capped columns has been reported (Lawson et al., 2010). In aged anvils, columns , plates, and small aggregates are observed near -43°C while larger aggregates are then found at lower altitudes (-36°C). Also in the cirrus part of MCS bullet-rosettes (more common for in situ cirrus (Lawson 2010)) and chain-like aggregates are found (aggregates of small rimed droplets caused by electric fields: Gayet et al., 2012; Stith et al., 2014).

With respect to ice particle density, Heymsfield et al., (2010) reported that ice particles seem to be denser near the convective part of MCS formed during the African Monsoon. Other studies have shown a variability of the mass-size relationship with temperature and related altitude (Fontaine et al., 2014; Schmitt and Heymsfield, 2010), which appears to be essentially linked to the variability of ice hydrometeor shapes related to different growth regimes (vapour diffusion, riming, aggregation).

Due to above mentioned spatiotemporal variations of MCS the different mean tendencies (hydrometeor concentration, ice water content, coefficients of mass-size relationship) reported in former studies can be partly linked to the chosen observation strategy of the MCS (i.e flight track in MCS) which of course is related to particular objectives of respective field projects (i.e. improvement of rain rate retrieval from satellite observations, icing condition at high altitude, comparison with ground radar observations, etc…).

Therefore the goal of this study is to investigate on the one hand the vertical variation of ice crystal properties in MCS (for example as a function of temperature) and on the other hand to study horizontal trends of ice microphysics at constant temperature levels. The latter will be accomplished by a composite analyses of microphysical properties and simultaneously measured radar reflectivity factor (Z). A frequency distribution of the profiles of the radar reflectivity factor throughout the MCS as a function of temperature allows to divide the microphysical in situ measurements into eight zones. For these height reflectivity zones microphysical properties are analysed and compared between the eight zones, but also intercompared between different locations and associated measurement campaigns where MCS were observed. Direct applications of this study are for example to improve retrievals of cloud properties from radar observations and also parameterization of ice properties in weather and climate models. Moreover, it can help identifying zones in MCS where numerical weather predictions ~~fails~~ in representing ice microphysics.

The statistical analysis includes more than 55844 data points of 5 s measurement duration in the temperature range from 215K to 273.15K. The following second section describes the utilized datasets and their derived parameters used in this study. The third section presents the analysis of radar reflectivity factors Z and retrieved vertical velocity (w_{ret}) profiles as a function of temperature T from the measurements of the 94GHz Doppler radar. Moreover, we will define the range of T and Z for which the intercomparison of microphysical properties will be performed. Section 4 then will present the results of the intercomparison of ice hydrometeor properties in tropical MCS. The last section adds the discussion and conclusion.

https://doi.org/10.5194/acp-2019-502
Preprint. Discussion started: 21 June 2019
© Author(s) 2019. CC BY 4.0 License.

Atmospheric Chemistry and Physics Discussions

2 Data description

This study uses a dataset where MCS were observed in 4 different locations over the world. Four locations in the tropics and related to two different projects:

1. Megha-Tropiques in Niamey, during July and August 2010: observation of continental MCS formed over the region of Niamey (Niger) during the West African Monsoon (Drigeard et al., 2015; Fontaine et al., 2014; Roca et al., 2015). 7665 points of 5 seconds.
2. Megha-Tropiques in Maldives, during November and December 2011: observation of oceanic MCS developed over the southern part of the Maldives and related to the ITCZ (Inter Tropical Convergence Zone) in the Indian Ocean. (Fontaine et al., 2014; Martini et al., 2015; Roca et al., 2015). 3347 points of 5 seconds.
3. HAIC-HIWC in Darwin, from January to March 2014: observations of MCS formed over Darwin and the North-East cost of Australia during the North Australian Monsoon (Leroy et al., 2016; Protat et al., 2016; Strapp et al. 2016; Leroy et al. 2017, Fontaine et al. 2017). 23265 points of 5 seconds.
4. HAIC-HIWC in Cayenne during May 2015: observations of MCS developed over the French Guyana during the peak of its raining season. 21567 points of 5 seconds (Yost et al., 2018).

All four measurement campaigns were conducted with the French research aircraft Falcon-20 operated by SAFIRE (Service des Avions Francais Instrumentés pour la Recherche en Environnement). On board the Falcon 20 were mounted two optical array probes (OAP): the 2D-S (2D stereographic probe; Lawson et al., 2006) and PIP (Precipitation Imaging Probe; Baumgardner et al., 2011), the cloud radar RASTA operating at 94GHz (Protat et al., 2016; Delanoë et al., 2014). In addition, bulk IWC measurements performed with the IKP-2 probe (Strapp et al. 2016; Davison et al. 2010) were available for the HAIC-HIWC flight campaigns (Darwin and Cayenne).

Both OAP probes record black and white images of hydrometeors with a resolution of 10µm and 100µm (2D-S and PIP, respectively). They are used to derived the size of hydrometeors (D_{max} [cm] in this study), their projected surface (S [cm^2]), their concentrations as a function of their size ($N(D_{max})$ [#/L/µm]). The sizes of hydrometeors span from 10 µm to 1.28 cm with Dmax calculated as a function of the projected surface of hydrometeors (taking the maximum of radius passing through its barycentre).

The IKP-2 probe was used to measure total condensed water, composed almost exclusively of ice water content (IWC [g m^{-3}]) during the HAIC-HIWC campaigns. For both Megha-Tropiques campaigns, IWC was retrieved using simulations of the reflectivity factor Z, thereby using the approximation of ice oblate spheroids (Fontaine et al. 2017; Fontaine et al., 2014). IWCs < 0.1g m^{-3} are not considered in this study, due to IKP-2 uncertainties particularly important for low IWC measurements (see Strapp et al. 2016a).

The 94GHz RASTA radar measures Z and Doppler velocity Vd below and above the aircraft. RASTA has 6 antennas that allow measuring three non-collinear Doppler velocities, from which the 3 wind components (including the vertical air velocity) have been reconstructed (using the Protat and Zawadzki 1999 3D wind retrieval technique modified for the aircraft geometry). ~~Accurate~~ description of data processing is documented in Leroy et al. (2016 and 2017), Protat et al. (2016), Strapp et al. (2016b), and Davison et al. (2016). The processing holds particularly for both datasets of the HAIC-HIWC project. The Megha-Tropiques datasets (Fontaine et al. (2014)) were reprocessed in order to undergo exactly the same version of processing tools for comparison reasons in this study.

3 Radar observations

3.1 Radar reflectivity factors

In this section distributions of radar reflectivity factors Z from nadir and zenith profiles are investigated for the 4 datasets. Figure 1 shows percentiles of Z as a function of T measured with RASTA during the 4 airborne campaigns. The lines are colour

https://doi.org/10.5194/acp-2019-502
Preprint. Discussion started: 21 June 2019
© Author(s) 2019. CC BY 4.0 License.

Atmospheric Chemistry and Physics Discussions

coded as a function of the calculated percentiles (blue =1th, light blue = 10th, cyan =30th, green=50th, yellow=70th, orange=90th, and red=99th percentile). Black lines represent the mean *Z* per flight campaign. Solid lines show results for the four datasets merged to one single global tropical dataset. These results are calculated using all vertical profiles of RASTA. *Z* for 30th and higher percentiles reveal a maximum around 265K. Figure 1 shows that the variability of *Z* at a given *T* is large. Also the probability to observe a certain value of *Z* is ~~is~~ different when comparing lower levels to higher ones. For example, *Z*≥10dBZ at 260K are encountered below the 70th percentile, whereas the same *Z* exists at 200K solely for few data points beyond the 99th percentile.

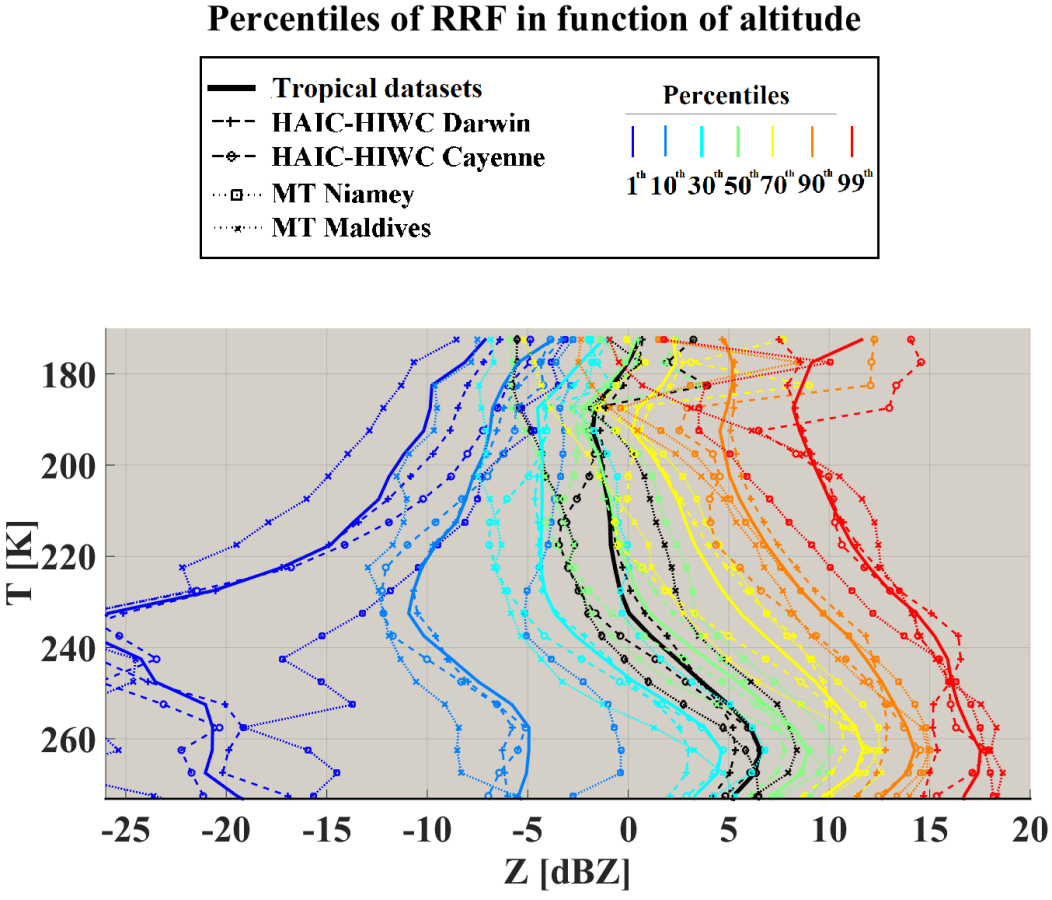

Figure 1: Median reflectivity factor *Z* and percentiles of radar reflectivity factors in dBZ on *x*-axis, as a function of temperature on *y*-axis.

The idea of this study is to compare the properties of ice hydrometeors for different tropical MCS locations, thereby rendering comparable different MCS systems (as a function of temperature), through the analysis of the frequency distribution of profiles of *Z* dividing all MCS into eight zones. Figure 1 shows that distributions of *Z* are not totally similar for all 5 airborne campaigns. This study is aware of the fact that the results are statistical results giving trends in microphysical properties, since for example *Z* is linked to the condensed water content (Fontaine et al., 2014; Protat et al., 2016), but also to the size distribution properties of total particle concentration, respective crystal sizes, and mean diameter (Delanoë et al., 2014). It has been clearly shown in former studies (for radar frequencies other than 94GHz) that in general higher *Z* are found in the convective zones of MCS, while the stratiform (or decaying) part of MCS tend to yield smaller *Z*. Indeed, Cetrone and Houze, (2009) used the profiling radar of TRMM satellite (Huffman et al., 2007) to demonstrate with frequency distributions of radar reflectivity *Z* as a function

https://doi.org/10.5194/acp-2019-502
Preprint. Discussion started: 21 June 2019
© Author(s) 2019. CC BY 4.0 License.

Atmospheric Chemistry and Physics Discussions

of height that higher *Z* occur more often in convective echoes of MCS (in West African Monsoon, Maritime Continent and Bay of Bengal) than in their stratiform echoes. Hence, this study presents ice microphysical properties in MCS as a function of temperature layers and also as a function of zones of reflectivity *Z*. In order to fix the limits of a limited number of *Z* levels, this study defines the percentiles of all merged campaign datasets shown by the solid lines (all data) in Figure 1. This defines *Z* ranges as a function of height. Hereafter, these ranges will be called MCS reflectivity zones and numbered 1 to 8:

- MCS reflectivity zone 1: $Z < Z^{1th}$
- MCS reflectivity zone 2 : $Z \in [Z(T)^{1th} ; Z(T)^{10th}[$
- MCS reflectivity zone 3 : $Z \in [Z(T)^{10th}; Z(T)^{30th}[$
- MCS reflectivity zone 4 : $Z \in [Z(T)^{30th}; Z(T)^{50th}[$
- MCS reflectivity zone 5 : $Z \in [Z(T)^{50th}; Z(T)^{70th}[$
- MCS reflectivity zone 6 : $Z \in [Z(T)^{70th}; Z(T)^{90th}[$
- MCS reflectivity zone 7 : $Z \in [Z(T)^{90th}; Z(T)^{99th}[$
- MCS reflectivity zone 8 : $Z \geq Z(T)^{99th}$

Figure 2 shows an example of the method to store data as a function of *T* and MCS reflectivity zones. In Figure 2(a), we can see original processed *Z* profiles for the flight 13 of HAIC-HIWC of the Darwin experiment. In Figure 2(b), eight colours representing the above defined MCS reflectivity zones. This method is applied for all datasets thereby using all radar reflectivity profiles (*Z* from Nadir and Zenith direction).

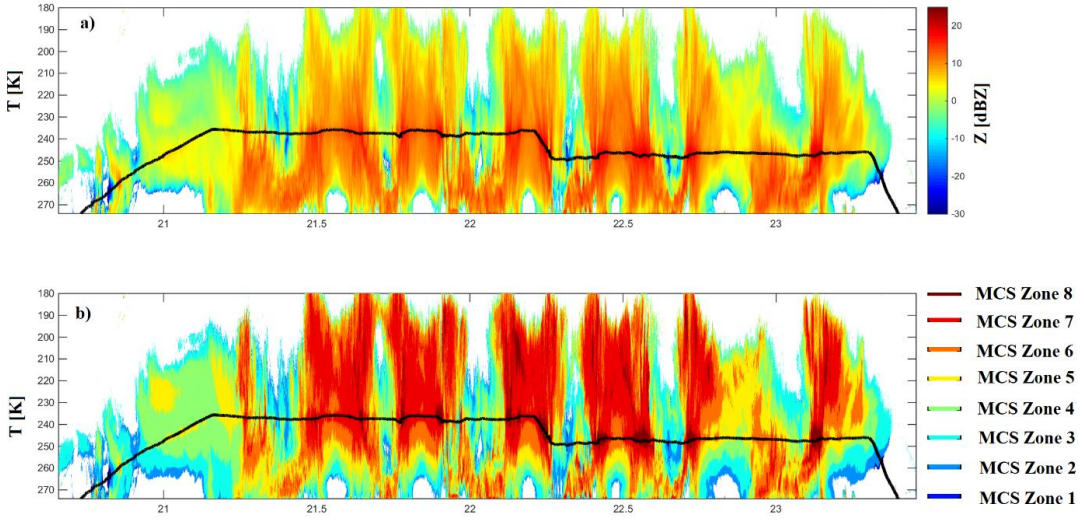

Figure 2: a) Time series of cloud radar profiles of flight 13 of HAI-HIWC at Darwin. Z color coded in dBZ and plotted as a function of the temperature (y-axis). b) Similar to a) with Z classified according to altitude dependent Z percentile ranges.

3.2 Retrieved vertical velocity

This section investigates links between retrieved vertical velocity and MCS reflectivity zones. We assume that *Vz* (V_d) = w_{ret} + *Vt*, where *Vt* is the terminal velocity of hydrometeors (Delanoë et al., 2007, 2014) and w_{ret} the vertical wind speed. Then, knowing *T* and *Z*, a probability to observe $| w_{ret} | \geq 1 m s^{-1}$ can be calculated as a function of MCS reflectivity zones and temperature (Figure 3; note that temperature for RASTA profiles stems from reanalysis of the ECMWF). In general, the probabilities to observe $| w_{ret} | \geq 1 m s^{-1}$ are highest for MCS reflectivity zones 8 then 7 and 6, meaning that these MCS

https://doi.org/10.5194/acp-2019-502
Preprint. Discussion started: 21 June 2019
© Author(s) 2019. CC BY 4.0 License.

Atmospheric Chemistry and Physics Discussions

reflectivity zones tend to be more impacted by convective areas of MCS, than is the case for other MCS reflectivity zones. Also, these probabilities generally increase with altitude for all airborne campaigns. Generally, in MCS reflectivity zones 5, 4, 3, and 2, the probabilities $P(|w_{ret} \geq 1|)$ as a function of T are close to each other with a decreasing trend as reflectivity decreases, except for the Maldives campaign, which may be due to significantly decreased statistics of very small local convective systems. Clearly MCS reflectivity zones 8 and 7 represent for all 4 datasets the more convective part of observed MCS and the lower reflectivity zones the more stratiform part with significantly lower vertical wind speeds.

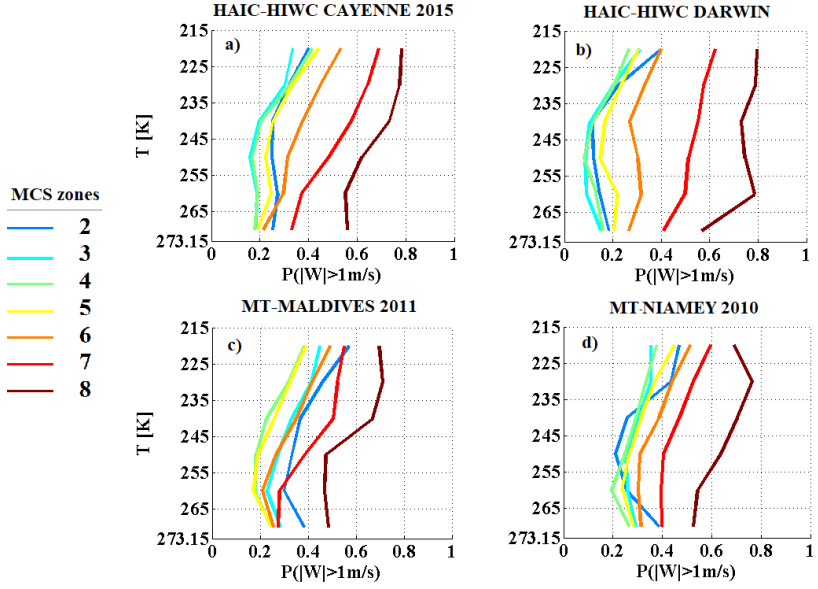

Figure 3 : Probability to observe magnitude of retrieved vertical air velocity larger than 1m s^{-1}, from measured Doppler velocity. Probabilities (x-axis) calculated as functions of MCS reflectivity zones 2 to 8 and plotted as a function of T (y axis). a) HAIC-HIWC in Cayenne, b)HAIC-HIWC in Darwin, c) Megha-Tropiques in Maldives Islands and d) Megha-Tropiques in Niamey.

The median magnitude of updraft ($w_{ret} \geq 0$) and downdraft wind speeds ($w_{ret} < 0$) are shown in Figure 4. Magnitudes of vertical velocity (negative and positive) are highest for MCS reflectivity zones 8. In general the updraft and downdraft wind speeds increase with altitude, which is in agreement with the probabilities $P(|w_{ret} \geq 1|)$ of Figure 3. For all 4 datasets vertical wind speeds of MCS reflectivity zones 2-6 are small with a consistent trend of decreasing vertical winds with decreasing radar reflectivity factors, except for the Maldives campaign (see also Figure 3). For MT-MALDIVES and MT-Niamey campaigns, wind speeds of MCS reflectivity zone 7 are small and rather close to what is observed for MCS reflectivity zones 2-6. However, for both HAIC-HIWC campaigns, the differences of vertical velocities between MCS reflectivity zone 7 and MCS reflectivity zones 2-6, are more pronounced than is the case for the two Megha-Tropiques campaigns.

In general, higher IWC and Z tend to be related with higher velocities, making MCS reflectivity zones 7 and 8 good candidates to represent microphysical properties of the most active zones of deep convective systems.

https://doi.org/10.5194/acp-2019-502
Preprint. Discussion started: 21 June 2019
© Author(s) 2019. CC BY 4.0 License.

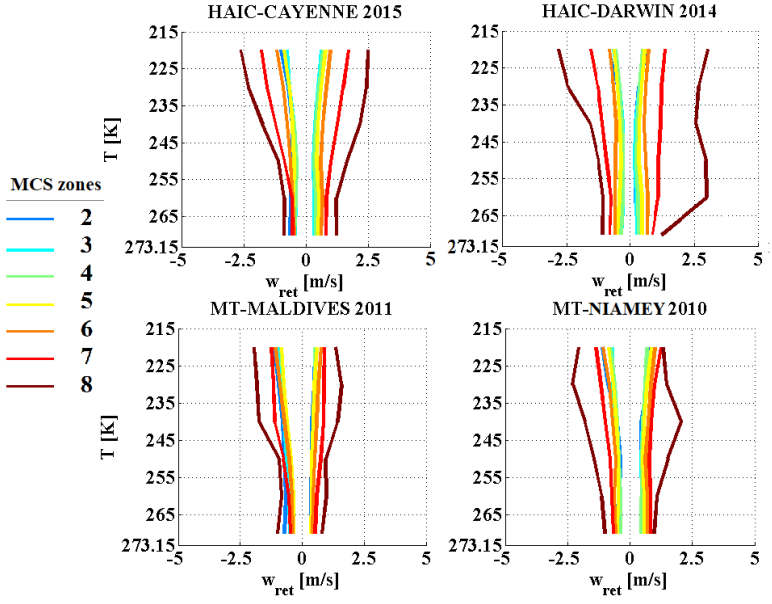

Figure 4: Retrieved median vertical velocity w_{ret} (from Doppler velocity) for all different MCS reflectivity zones and as a function of temperature T, with same color code as in Figure 2. Velocity is given in m s^{-1} on x-axis and T in K on y-axis. Median velocity value calculations are performed for positive velocity (upward) and negative velocity (downward), separately.

4 Method of intercomparison

This study compares and discusses a series of ice cloud properties, such as IWC, visible extinction, α and ß coefficients of the dynamically retrieved m(D) power law, large crystal proxy of PSDs, crystal number concentrations N, PSD 2nd and 3rd moments (M_2 and M_3, respectively), and the ratio of IWC/M_2. The above mentioned ice hydrometeor properties in all 4 MCS locations will be investigated as a function of T and MCS reflectivity zones (range of Z given by percentiles of Z as a function of T) which have been introduced in section 3. In the subsequent section 5 a series of figures presenting results for above mentioned ice cloud properties (parameter X) will be presented in a uniform format (Figures 5, 6, 8, 9, 10, 11, 12, 13, 14, 15 and 16). In all these figures, the sub figures noted (a), show the median values of X, averaging MCS data from the 4 tropical campaigns (with 25th and 75th percentiles represented by whiskers), as a function of T and MCS reflectivity zones. If the range of variability of this median of parameter X in MCS reflectivity zone $\boldsymbol{i}$ defined by its 25th and 75th percentiles, does not overlap with corresponding ranges of variability of X defined by the 25th and 75th percentiles of MCS reflectivity zones $\boldsymbol{i}$-1 and $\boldsymbol{i}$+1, respectively, this makes the median (4 tropical campaigns) of X a candidate for X parametrization as a function of MCS reflectivity zone and T. We call these figures (a) the "tropical dataset". Then, in sub-figures (b), (c), (d) and (e), we calculate the median relative difference in percent (hereafter MRD-X) for all 4 individual MCS datasets (CAYENNE, DARWIN, MALDIVES, and NIAMEY) with respect to the median of X as a function of MCS reflectivity zone and T.

In order to take into account the uncertainties in all type of measurements, uncertainties (hereafter noted $U(X)/X$) for each parameter X were taken from Baumgardner et al. (2017). When the MRD-X is larger than $U(X)/X$, this means that there is a significant difference between the median of the studied parameter for the tropical dataset and the respective X of the selected individual MCS dataset. For the case that MRD-X is smaller than or equal to $U(X)/X$, the median of X of the tropical dataset, under the condition that the median (4 tropical campaigns) of X is distinguishable between neighboring MCS reflectivity zones, can be utilized for the respective type of MCS. Hence, if the latter case is true for all 4 MCS locations, then the median (4 tropical campaigns) of X is suitable to represent all 4 types (=location) of observed MCS.

https://doi.org/10.5194/acp-2019-502
Preprint. Discussion started: 21 June 2019
© Author(s) 2019. CC BY 4.0 License.

Atmospheric Chemistry and Physics Discussions

Note that in all figures (Figures 5, 6, 8, 9, 10, 11, 12, 13, 14, 15 and 16) temperature of in-situ observations will be on the y axis and the color coded MCS reflectivity zones correspond to RASTA reflectivity statistics as a function of temperature. Measured/calculated parameters *X* are sorted into MCS reflectivity zones according to Z derived at flight level simultaneously to measured/calculated *X* parameter. The grey band in sub-figures (a) shows 25th and 75th percentiles of the parameter for the entire tropical dataset thereby merging data from all MCS reflectivity zones.

25th, median, and 75th percentiles of all parameters presented in the figures for the tropical dataset are given in ~~Annexe~~ A, in order to allow comparison with other datasets and evaluation of numerical weather prediction models.

The comparison of ice hydrometeors' properties of the 4 MCS locations investigated in this study, will mainly focus on the question, if MRD-*X* (for individual MCS reflectivity zones) is larger or smaller than *U(X)/X*, also depending on MCS locations.

5 In-situ Observations in tropical MCS: HAIC-HIWC and Megha-Tropiques projects

5.1 Ice water content

Figure 5 shows measured IWC from IKP-2 for HAIC-HIWC campaigns over Darwin and Cayenne, then IWC retrieved from T-Matrix simulations of Z for both Megha-Tropiques campaigns over Niamey and the Maldives Islands. Figure 5(a) shows median IWC as a function of T for 4 datasets plus one median curve for the merged 4 tropical datasets (subsequently called global dataset). Also median IWC for individual MCS reflectivity zones are presented for the merged tropical dataset. Solely, the graphical representation is limited to medians of IWC for MCS reflectivity zones 4 to 8. Indeed, IWC in MCS reflectivity zones 2 and 3 are linked to IWC smaller than 0.1 g m^{-3}, where IWC data are subject to less confidence. Globally, 30% of the data observed in 4 tropical MCS have an IWC lower than 0.1g m^{-3}, and the lower limit of MCS reflectivity zone 4 is defined with the 30th percentiles of Z. The figure reveals an IWC increases with increasing MCS reflectivity zone for a given range of temperature. IWC median values differ clearly as a function of the MCS reflectivity zone, and this for the entire range of temperatures, with only a few exceptions above the freezing level ($T \in$ [265 K; 273 K[), between MCS reflectivity zones 4 and 5, and MCS reflectivity zones 7 and 8, respectively, with small overlap in IWC ranges. In MCS reflectivity zones 4 to 7, median IWC increase with increasing T between 215 K and 260 K (where IWC has its maximum) and then slightly decrease as T further increases towards 273K. In MCS reflectivity zone 8 IWC behaves rather similar with a maximum IWC already reached at 250 K.

In Figure 5 (b) Figure 5 (c) the grey band area displays the IWC uncertainty of the IKP-2 measurements (*U(IWC)/IWC*; Strapp et al. 2016; Leroy et al. 2016; Fontaine et al. 2017). This uncertainty decreases with altitude to less than 10% at 210K. The grey band area in Figure 5(d) Figure 5(e) shows the estimated uncertainty (of ±32% of IWC from IKP-2) of IWC retrieved from T-matrix simulations of the reflectivity factor, approximating ice crystals with oblate spheroids (Fontaine et al., 2017). This means that confidence in direct bulk IWC measurements from the IKP-2 is significantly higher than in indirect IWC calculations from T-matrix simulations.

https://doi.org/10.5194/acp-2019-502
Preprint. Discussion started: 21 June 2019
© Author(s) 2019. CC BY 4.0 License.

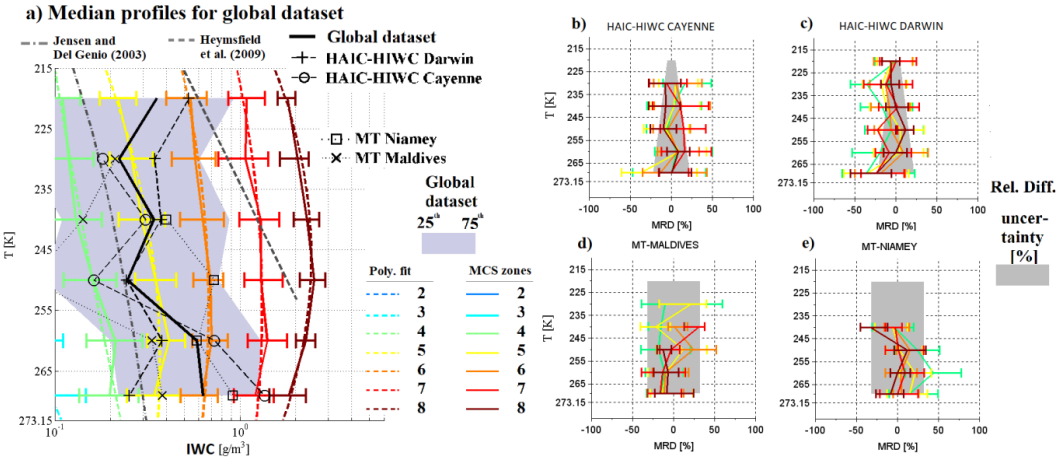

Figure 5: a) Median of IWC in [g/m^3] on x-axis, as a function of temperature in [K] on y-axis for different MCS reflectivity zones. Results for the global tropical dataset including both MT and both HAIC-HIWC datasets. The grey band represents 25th and 75th percentiles of global dataset. Median relative difference (MRD) of IWC during b) HAIC-HIWC in Cayenne, c) HAIC-HIWC in Darwin, d) Megha-Tropiques Maldives Islands and e) Megha-Tropiques in Niamey, with respect to median of IWC for the Tropical dataset on x-axis as a function of temperature in [K] on y-axis. The grey bands represent the uncertainties of the IWC measurement in b) and c), and the median deviation between measurement and the IWC retrieval method (Fontaine et al. 2016) in d) and e). Lines are colored as a function of the MCS reflectivity zones where in-situ measurement were performed, dashed colored lines are corresponding to the polynomial fit. Extremity of error bar show 25th and 75th percentiles of IWC relative error in each MCS reflectivity zone.

In addition, Figure 5(b), (c), (d), and (e) show MRD-IWC for all MCS reflectivity zones as a function of T. For all 4 tropical MCS, MRD-IWC in MCS reflectivity zones 4 to 8 are distributed around 0 and are in general less than 30-40% (25th to 75th percentiles). Measured IWC in MCS reflectivity zone 8 are in particular good agreement with the median IWC for all 4 tropical datasets, except maybe for high altitude MT-Niamey data. Uncertainty U(IWC)/IWC for IKP-2 measurements (Darwin and Cayenne) especially at high altitude (about 5%) is smaller than the expected deviation MRD-IWC. For mid and lower altitudes, MRD-IWC for Darwin and Cayenne particularly for zones 5 and 8 are of the order of corresponding U(IWC)/IWC. Concerning, MCS over Niamey and the Maldives Island, MRD-IWC (25th to 75th percentiles) in general do not exceed corresponding U(IWC)/IWC.

For comparison purposes with former studies, two IWC-T relationships from literature are added in Figure 5(a). Jensen and Del Genio (2003) suggested an IWC-T relationship in order to account for the limited sensitivity of the precipitation radar aboard the TRMM satellite, not allowing for small ice crystals at the top of convective clouds' anvils to be observed. They used radar reflectivity factors of a 35GHz radar based on Manus Island (North-East of Australia; 2.058°S, 147.425°E), thereby calculating IWC from an IWC-Z relationship (IWC=0.5*(0.5.Z$^{0.36}$); Jensen et al., 2002). The resulting IWC-T relationship given by Jensen and Del Genio (2003) is reported by a dashed-dotted grey line, which fits between 75th percentiles of tropical median IWC of MCS reflectivity zone 4 and 25th percentile of MCS reflectivity zones 5. We recall that IWC, as a function of T, in MCS reflectivity zones 4 and 5 are related to Z between 30th-50th and 50th-70th percentiles, respectively. We may notice that the IWC-T relationship from Jensen and Del Genio (2003) is different and smaller than the median IWC (4 tropical campaigns).

Moreover, (Heymsfield et al., 2009) established an IWC-T relationship based on 7 fields campaigns (dashed grey line in Figure 5(a). They focused their study on maritime updrafts in tropical atmosphere for a temperature range T $\in$ [213.15K; 253.15K]. Their suggested IWC tend to be in the range of IWC of MCS reflectivity zones 6- 8 with IWC increasing with T. We already showed in section 3.2 that MCS reflectivity zones 7 and 8 have higher probabilities to be convective (updraft regions with higher magnitudes of vertical velocity), as compared to other MCS reflectivity zones. Therefore, (Heymsfield et al., 2009) IWC parametrizations for maritime updrafts are not inconsistent with data from this study.

https://doi.org/10.5194/acp-2019-502
Preprint. Discussion started: 21 June 2019
© Author(s) 2019. CC BY 4.0 License.

Atmospheric Chemistry and Physics Discussions

Overall, this section demonstrates that variation of IWC with the temperature is similar in all type of MCSs for corresponding ranges of radar reflectivity factors. Hence, IWC-Z-T relationships developed in Protat et al., (2016) is usable for all types of MCS in the Tropics, at least for IWC larger than 0.1g m^{-3}.

5.2 Visible extinction

Figure 6 shows visible extinction coefficients (σ) calculated from OAP 2D images (approximation of large particles; Van de Hulst, 1981):

$$\sigma = 2 \cdot \sum_{15\mu m}^{12845\mu m} N(D_{max}) \cdot S(D_{max}) \cdot \Delta D_{max} \quad [m^{-1}] \tag{1}$$

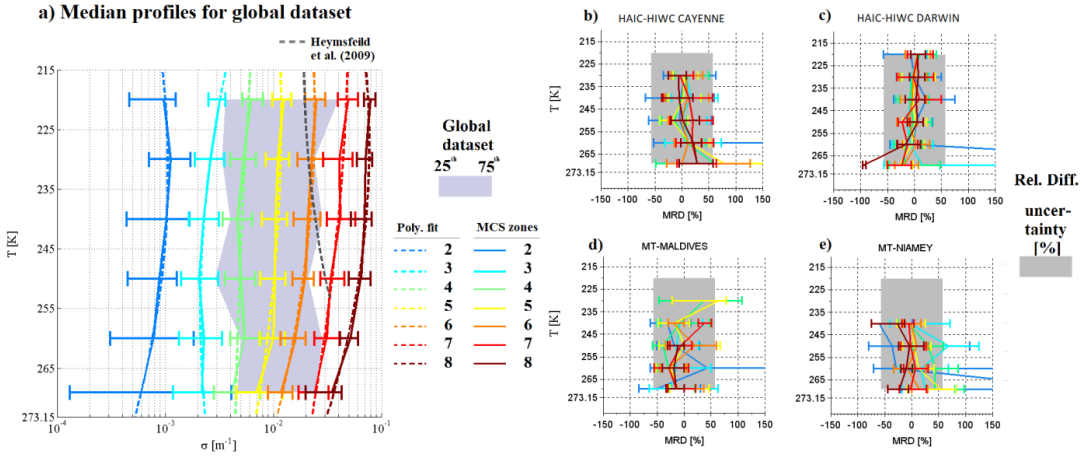

Figure 6: Same as Figure 5 but for visible extinction σ given on x-axis in m^{-1}.

In Figure 6(a), median σ (4 tropical campaigns) increase with MCS reflectivity zone as expected, and also increase with altitude (decrease with T), with larger gradients for T ∈ [245; 273.15] than for T ∈ [215K; 245K].

The uncertainty (U(σ)/σ) (grey band in Figure 6(b) to Figure 6(e) is calculated as follows:

$$\frac{U(\sigma)}{\sigma} = \sqrt{2 \cdot \frac{U(D)^2}{D} + \frac{U(N)^2}{N}} = \pm 57\% \tag{2}$$

With $\frac{U(D)}{D} = \pm 20\%$, taking into account the uncertainty in the calculation of the size of hydrometeors and $\frac{U(N)}{N} = \pm 50\%$ for the uncertainty on the calculation of the concentration of hydrometeors from optical array probes (Baumgardner et al., 2017). Above uncertainties are those for particles larger than 100 µm. Note, that if we took uncertainties for particles smaller than 100µm (with $\frac{U(D)}{D} = \pm 50\%$ and $\frac{U(N)}{N} = \pm 100\%$) the uncertainty on the calculation of σ would increase to ± 122%.

For all 4 types of tropical MCS, MRD-σ shown in Figure 6(b), 6(c), 6(d), and Figure 6(e) are in general smaller or equal to $\pm\frac{U(\sigma)}{\sigma}$. Hence, visible extinction in tropical MCS tend to be similar for all types of MCS observed in the same range of *T* and MCS reflectivity zone. Also MRD-σ trends are very comparable to above discussed MRD-*IWC* trends.

Furthermore, a σ–*T* relationship from Heymsfield et al. (2009) (grey dashed line) is added in Figure 6 (a), which is calculated, as a function of *T*, as the sum of the total area of particles larger than 50µm plus the total area of particles smaller than 50µm multiplied with a factor of 2 in order to satisfy Eq. (1) and to compare with results of this study. We conclude that σ–*T* estimation presented in Heymsfield et al. (2009) for maritime convective clouds is rather comparable to median MRD-σ calculations (4 tropical campaigns) in MCS reflectivity zones 6 to 7 corresponding to higher reflectivity zones, and thus statistically to zones with some remaining convective strength.

https://doi.org/10.5194/acp-2019-502
Preprint. Discussion started: 21 June 2019
© Author(s) 2019. CC BY 4.0 License.

Atmospheric Chemistry and Physics Discussions

Since we concluded from Figure 6 that extinction σ in tropical MCS tend to be similar for all MCS locations in the same range of T and for corresponding MCS reflectivity zones, a parametrization for σ is given in equation (3) below, which presents a fit of $ln(\sigma)$ as a function of IWC and T for deep convective cloud data (4 tropical campaigns) of this study limiting data to IWC > 0.1g m^{-3}:

$$ln(\sigma) = -0.0194587 \cdot T + 0.9134019 \cdot ln(IWC) + 1.2423609 \quad (3)$$

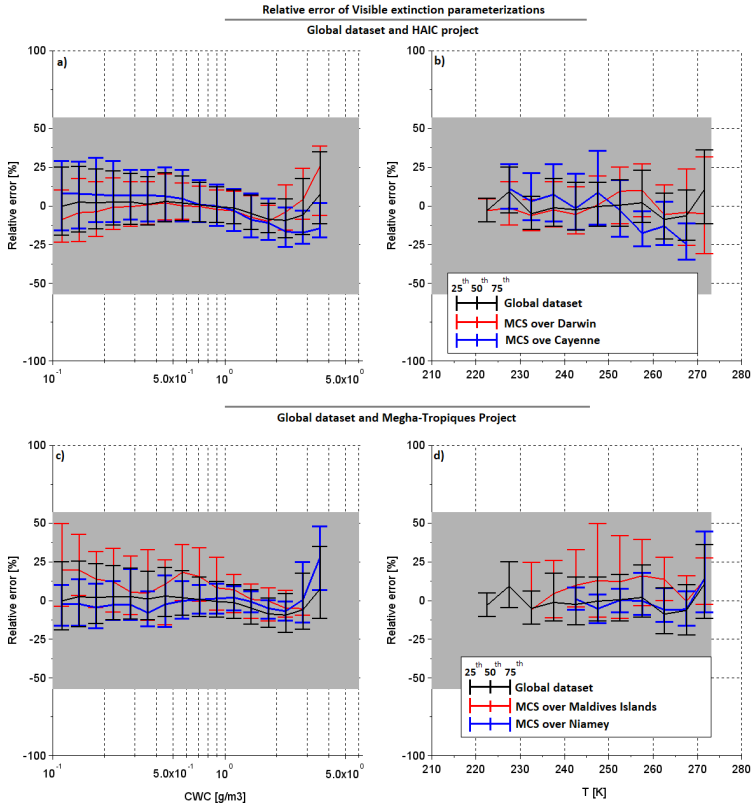

Figure 7: Relative errors of predicted visible extinction Eq. (3) with respect to measured visible extinction for a), b), c), and d. Relative errors as a function of IWC in a) and c) and as a function of T in b) and d). Black lines in 4 sub figures represent the relative errors when calculated for the entire tropical dataset. In a) and b) red lines show median relative error for MCS over Darwin, and blue line for MCS over Cayenne. In c) and d) red line represent median relative errors for MCS over Maldives Islands and blue lines for MCS over Niamey. Bottom of error bar shows 25th percentiles of relative errors and 75th percentiles are given by top of error bar.

An evaluation of this parametrization is presented in Figure 7, where black lines in 7-a) to 7-d) represent median relative errors of σ (with 25th and 75th percentiles represented by whiskers) for the global tropical dataset predicted with Eq. (3) with respect to retrieved σ from OAP images from Eq. (2). In addition, median relative errors of σ for individual MCS datasets over Darwin, Cayenne, Maldives Islands, and Niamey with respect to σ calculations (Eq. (3)) are shown in Figure 7(a), 7(b), Figure 7 (c), and 7(d), respectively. The uncertainty $\pm \frac{U(\sigma)}{\sigma}$ is given with the grey band. All relative errors (25th - 75th percentiles) tend to be smaller than $\pm \frac{U(\sigma)}{\sigma}$, with median relative errors that are smaller than ±25% of σ uncertainty calculated from Eq. (2). In general, Eq. (3) seems to produce smallest relative errors of σ for Niamey and Darwin datasets (especially for IWC<2g m^{-3}).

To sum up, visible extinction calculated from equation (1) shows similar behavior for all four types of tropical MCS. Indeed, for the same range of temperature and radar reflectivity factors we find very comparable visible extinction in all 4 MCS locations, thereby taking into account the measurement uncertainty. Similar results as for the visible extinction has been

https://doi.org/10.5194/acp-2019-502
Preprint. Discussion started: 21 June 2019
© Author(s) 2019. CC BY 4.0 License.

Atmospheric Chemistry and Physics Discussions

documented in the previous section for IWC. From those two results, we can assume that in MCS zones where IWC is larger than 0.1g m^{-3} hydrometeor populations are similar in shape and density. This is why the development of a parameterization of the visible extinction as a function of temperature and IWC (beyond 0.1g m^{-3}) has been presented (see equation (3)). Noteworthy, optically thick clouds are responsible of large errors in retrieved cloud water path and condensed water concentration profiles retrieved from satellite imageries (Smith, 2014; Yost et al., 2010). Parameterizations, such as presented here, could help to improve retrieval methods on cloud water path and more investigations on the benefit of such parameterizations are needed, which is beyond the scope of this study.

5.3 Concentration of ice hydrometeors

Subsequently are presented observed total concentrations (N_T) for the tropical datasets integrating particle sizes beyond 15µm:

$$N_T = \sum_{Dmax=15}^{Dmax=12845} N(D_{max}) \cdot \Delta D_{max} \qquad [L^{-1}] \tag{4}$$

Figure 8 (a) shows median N_T as a function of T and MCS reflectivity zone. Median N_T systematically increase with MCS reflectivity zone and altitude, however with significant overlap of 25th and 75th percentiles of neighboring MCS reflectivity zones. Measurement uncertainty on concentrations given for small hydrometeors is about ±100% (Baumgardner et al., 2017). Figure 8 (b), 8(c), 8(d), and 8(e) show MRD-N_T of MCS in different tropical locations. For MCS over Darwin and Cayenne, in all MCS reflectivity zones MRD-N_T are smaller than the measurement uncertainty, whereas for Niamey data this is the case only in MCS reflectivity zones 2, 5, 6 and 7. MCS over Maldives Islands yield significantly larger MRD-N_T than the measurement uncertainty, and those are primarily positive. Hence, MCS over Maldives Islands have larger concentrations of hydrometeors for a same range of T and Z, than the three other types of tropical MCS. However, these larger concentrations observed do not concern zones where highest concentrations of hydrometeors were observed. For example, in MCS reflectivity zone 4 where MRD-N_T is reaching 1000%, N_T for the Maldives dataset are approximately 1000 L^{-1}, which is similar to N_T observed in MCS reflectivity zones 7 and 8 for the same range of T ∈ [235K; 245K[for the global dataset. We recall that identical image data processing to remove shattering artefacts and to correct for out of focus images (Field et al., 2003; Korolev and Isaac, 2005; Leroy et al., 2016) have been applied for all 4 tropical datasets. Also the presence of super cooled droplets has been investigated (RICE, CDP probe), and few periods with super cooled water content have been removed for this study. Moreover, we will see section 5.5 that MCSs over Maldives Islands tend to have smaller $max(D_{max})$ especially in MCS reflectivity zones 4, 5, 6 and 7 compared to the other MCS locations and that concentrations beyond 500µm in Maldives Islands observations are in the same range as the other types of MCS.

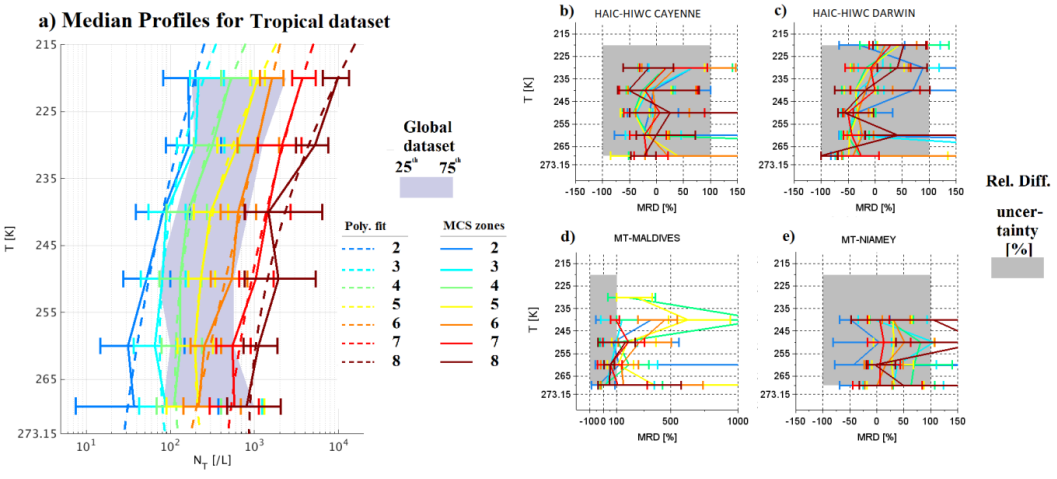

https://doi.org/10.5194/acp-2019-502
Preprint. Discussion started: 21 June 2019
© Author(s) 2019. CC BY 4.0 License.

Atmospheric Chemistry and Physics Discussions

Figure 8: Same as Figure 5, but for concentrations of hydrometeors integrated beyond D_{max} =15µm in [L^{-1}].

In order to mitigate the impact of PSD uncertainties related to smallest hydrometeor sizes (shattering and other artefacts in combination with very small sample volume of smallest particles), we now compare total concentrations of hydrometeors beyond 55µm ($N_T(D_{max} > 55\mu m)$; hereafter $N_{T,55}$):

$$N_T(D_{max} > 55\mu m) = \sum_{Dmax=55}^{Dmax=12845} N(D_{max}) \cdot \Delta D_{max} \qquad [L^{-1}] \tag{5}$$

Median of $N_{T,55}$ as a function of T and MCS reflectivity zones are shown in Figure 9 (a) as well as MRD-$N_{T,55}$ for the 4 tropical MCS locations in Figure 9 (b), 9(c), 9(d), and 9(e). The findings for $N_{T,55}$ are similar to those for median N_T, with an increase of median $N_{T,55}$ with altitude for all MCS reflectivity zones. Also $N_{T,55}$ increases with MCS reflectivity zones for a given T, with highest $N_{T,55}$ in MCS reflectivity zone 8. As for N_T, the range of variability for $N_{T,55}$ reveals significant overlap of 25th and 75th percentiles of neighboring MCS reflectivity zones. Even if the limit of concentrations of ice hydrometeors are not well defined between neighboring MCS reflectivity zones, these concentrations tend to be similar for a given range of T and Z for different MCS locations.

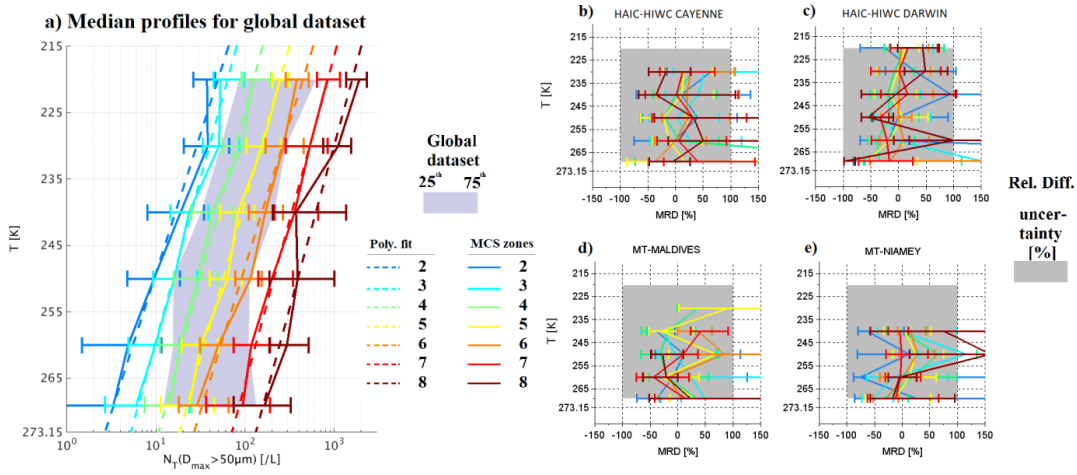

Figure 9: Same as Figure 5, but for total concentrations integrated beyond D_{max}=55µm in [L^{-1}].

Globally, median of $N_{T,55}$ for the tropical dataset are smaller by about one order of magnitude with respect to the median of N_T for the same MCS reflectivity zone. Measurement uncertainty on concentrations are again assumed ±100%. MRD- $N_{T,55}$ in 4 different tropical MCS locations, particularly for higher MCS reflectivity zones are of the order and even larger (75th percentile MRD-$N_{T,55}$) than the measurement uncertainty. Finally, Figure 10 shows concentrations of hydrometeors when number PSD are integrated only beyond 500µm (hereafter $N_{T,500}$; eq. (6)), where the uncertainty on their measurement is estimated as about ±50% for hydrometeors larger than 100µm (Baumgardner et al., 2017).

$$N_T(D_{max} > 500\mu m) = \sum_{Dmax=505}^{Dmax=12845} N(D_{max}) \cdot \Delta D_{max} \qquad [L^{-1}] \tag{6}$$

https://doi.org/10.5194/acp-2019-502
Preprint. Discussion started: 21 June 2019
© Author(s) 2019. CC BY 4.0 License.

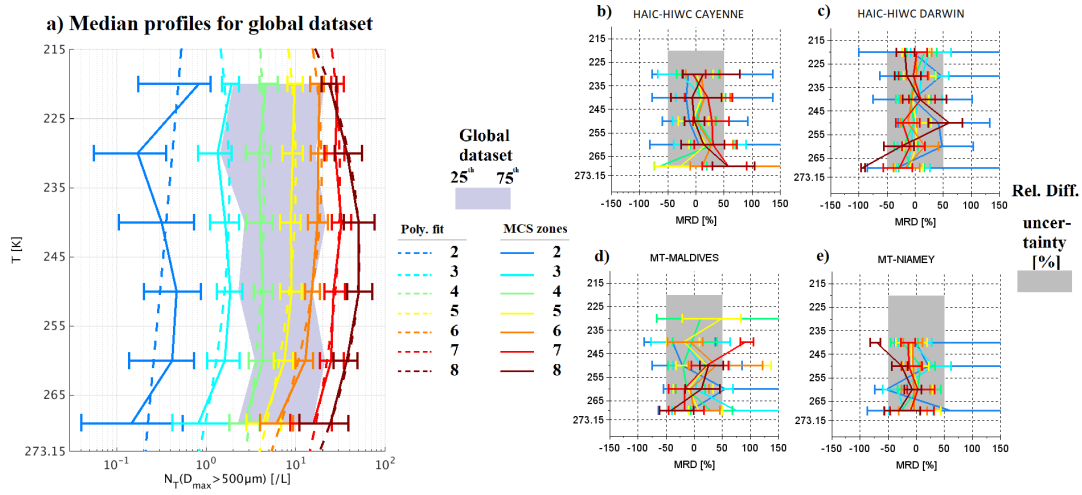

Figure 10: Same as Figure 5, but for concentrations of hydrometeors integrated beyond D_{max} =500µm in [L^{-1}].

In Figure 10 (a) median $N_{T,500}$ are presented as a function of T and MCS reflectivity zone. The curves of median $N_{T,500}$ are different from curves of median N_T and $N_{T,55}$. Indeed, particularly for higher MCS reflectivity zones and in lower altitude levels ($T \in$ [250K; 273.15K]), $N_{T,500}$ tends to increase with altitude, reaches a maximum value around $T \in$ [235K; 250K], and then rather decreases for $T \in$ [215K; 235K]. The range of variability for $N_{T,500}$ reveals a rather small overlap, if any, of 25th and 75th percentiles of neighboring MCS reflectivity zones 8, 7, and may be 6, mainly at coldest $T \in$ [215K; 225K]. No overlap for MCS reflectivity zones 2-5 and concentration of ice hydrometeors beyond 500µm are rather constant from 215K to 265K for observations in MCS reflectivity zones 3 to 5. We can assume that sedimentation does not significantly impact hydrometeors of sizes below 500 µm, but should impact larger hydrometeors. Figure 10 (b), 10(c), 10(d), and 10(e) reveal that MRD-$N_{T,500}$ in higher MCS reflectivity zones are considerably smaller or roughly equal to the measurement uncertainty for large hydrometeors. Some smaller exceptions are noticeable where MRD-$N_{T,500}$ are larger than the measurement uncertainty for very low altitudes at $T \in$ [265K; 273.15K[, namely Cayenne in MCS reflectivity zones 7 and 8, and Darwin in MCS reflectivity zone 8. Note, that in general MRD-$N_{T,500}$ have smaller 75th percentiles (from Figure 10 (b), 10(c), 10(d), and 10(e)) compared to respective MRD-$N_{T,55}$ and MRD-N_T, showing that variability in each MCS reflectivity zone for hydrometeors larger than 500µm is smaller than the variability of concentrations which include smaller ($N_{T,55}$) and smallest (N_T) hydrometeors. This finding is clearly related to the uncertainty estimation given by (Baumgardner et al., 2017)) that small hydrometeors ($D_{max}<$ 100µm) have a larger estimated uncertainty of 100% (due to shattering, very small sample volume), compared to the uncertainty of only 50% for larger hydrometeors ($D_{max}>$100µm). Hence, it is not surprising that variability around a median value is larger for N_T and $N_{T,55}$ than for $N_{T,500}$. It is important to ~~resume~~ here that not just MRD-$N_{T,500}$ is smaller than the uncertainty of 50%, but also that MRD-$N_{T,500}$ is tremendously smaller than MRD-$N_{T,55}$ and MRD-N_T. Even though we have to keep in mind that we'll never have sufficient statistics in flight data, due to sampling bias of flight trajectories and variability of microphysics from one system to another. Indeed, Leroy et al., (2017) demonstrated that median mass diameter MMD_{eq} generally decrease with T and increasing IWC for the dataset of HAIC-HIWC over Darwin. However, for two flights performed in the same MCS, Leroy et al., (2017) showed that high IWC were linked to large MMD_{eq}, where MMD_{eq} tends to increase with IWC. This demonstrates that comparable high IWC can be observed for two different microphysical conditions (short-lived typical oceanic MCS versus long lasting tropical storm in one and the same dataset).

We show that total concentrations starting from 15µm can be different between MCS locations as a function of T and Z, especially in oceanic MCS over Maldives Islands in the decaying part of these MCSs where measured concentrations can reach

https://doi.org/10.5194/acp-2019-502
Preprint. Discussion started: 21 June 2019
© Author(s) 2019. CC BY 4.0 License.

Atmospheric Chemistry and Physics Discussions

10 times the median concentrations observed globally for merged tropical dataset. Also MCS over Niamey show larger concentrations near the convective part of MCS. However, concentrations of ice hydrometeors beyond 55µm tend to be more similar as function of *T* and *Z*, even if the limits between each MCS reflectivity zones are not well defined.

Between 4 MCS locations, differences of aerosol loads and available ice nuclei might exist. Despite those possible differences, ice crystal formation mechanisms may be primarily controlled by dynamics, thermodynamics and particularly by secondary ice production rather than primary nucleation; (Field et al., 2016; Phillips et al., 2018; Yano and Phillips, 2011) that regulate the concentrations of hydrometeors beyond ~55µm making these concentrations quiet rather similar for different MCS locations.

5.4 Coefficients of mass-size relationship

The relationship between mass and size of ice crystals is complex. Usually in field experiments the mass of individual crystals is not measured, instead bulk IWC is measured which is the integrated mass of an ice crystal population per sample volume to be linked to PSDs of ice hydrometeors. Yet IWC is not always measured or with low accuracy. Due to the complex shape of ice hydrometeors, various assumptions allow to estimate the mass of ice crystals for a given size. Indeed, many habits of ice crystals can be observed in clouds, primarily as a function of temperature and ice saturation (Magono and Lee, 1966; Pruppacher et al., 1998). Also hydrometeors of different habits can be observed at the same time (Bailey and Hallett, 2009). Locatelli and Hobbs (1974) and Mitchell (1996) suggested mass-size relationships represented as power laws with $m = \alpha \cdot D^{\beta}$ for different precipitating crystal habits. Coefficients α and β vary as a function of the ice crystals habit. Further studies performed calculations of mean mass-size relationships (also using power law approximations) retrieved from simultaneous measurements of particle images combined with bulk ice water content measurements (Brown and Francis, 1995; Cotton et al., 2013; Heymsfield et al., 2010). Schmitt and Heymsfield (2010), Fontaine et al (2014), Leroy et al. (2016) showed that mass-size relationship coefficients α and β vary as a function of temperature. In the latter studies, coefficient β is calculated from OAP images, and then α is retrieved either also from processed images or constrained with integral measured IWC or radar reflectivity factor *Z*. Recently, Coutris et al (2017) retrieved masses of hydrometeors by an inverse method using direct measurement of PSD and IWC. In this latter study, the mass of ice crystals is retrieved without any assumption on the type of function linking mass and size of ice hydrometeors.

This study utilizes the power law assumption to constrain the mass of ice hydrometeors. Thereby, the β exponent of the mass-size power law relationship is calculated (eq. 7) as presented in Leroy et al (2016) for hydrometeors defined by D_{max} dimension:

$$\beta = 1.71 \cdot f_s - 0.62 \cdot f_p \quad (7)$$

Here f_p is the exponent of the perimeter-size power law relationship (Duroure et al. 1994) with $P(D_{max}) = e_p \cdot D_{max}^{f_p}$ $[cm]$ and f_s is the exponent of the 2D image area-size relationship (Mitchell, 1996) with $S(D_{max}) = e_s \cdot D_{max}^{f_s}$ $[cm^2]$. Figure 11(a) shows the variability of β as a function of temperature and MCS reflectivity zones for the global tropical dataset. For a given MCS reflectivity zone, β increases with increasing temperature. Also for a given temperature, β increases with MCS reflectivity zone, although MCS reflectivity zones 4, 5, 6, 7, and 8 share a range of common values for β, making it more uncertain to predict with a good accuracy using a parametrization as function of *Z* and *T* (as it has been done for extinction σ).

https://doi.org/10.5194/acp-2019-502
Preprint. Discussion started: 21 June 2019
© Author(s) 2019. CC BY 4.0 License.

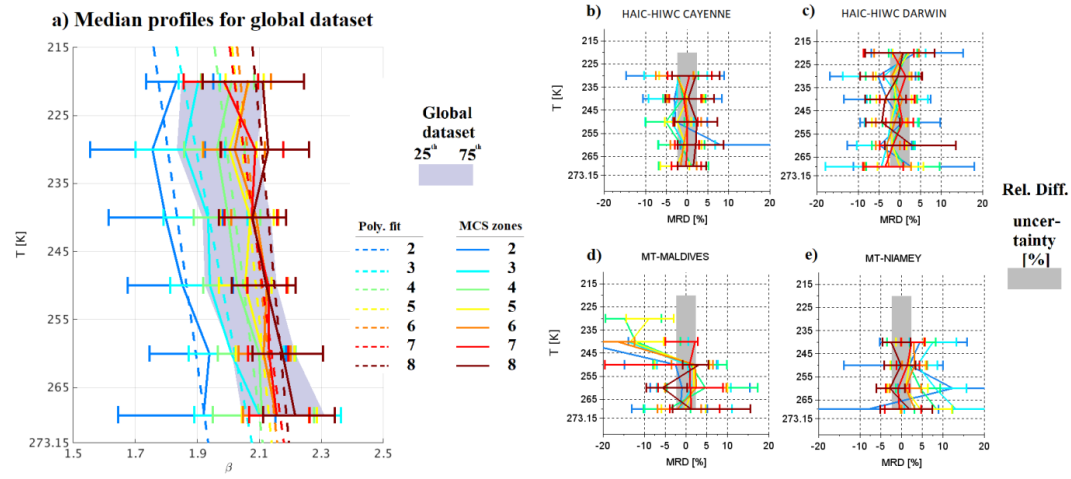

Figure 11: As Figure 5, but for exponent β of mass-size relationships for used ice hydrometeor size definition D_{max}.

In order to estimate the uncertainty on the calculation of β (grey band in Figure 11 (b), (c), (d), and (e), results from (Leroy et al., 2016) have been utilized, with $U(\beta)/\beta$=±2.3%. However, if we have calculated the uncertainty on retrieved β from the uncertainty on the measurement of the size and concentration of hydrometeors from OAP images, the uncertainty would have been by about 44%. Figure 11 (b), 11(c), 11(d), and 11(e) show in general that for higher MCS reflectivity zones MRD-β are smallest (5-10%) for Cayenne and Niamey, then with some restrictions also for Darwin data. MRD-β show larger values for data of the Maldives Islands which may be due to decreased statistics of only two observed MCS systems at the beginning of the campaign merged with subsequently sampled rather small local convective systems.

Overall, the predictability of β coefficients as a function of T and MCS reflectivity zone remains challenging. We are aware of the fact that the power-law approximation has certain limits, trying to impose one single β to an entire crystal population composed of smaller (dominated by pristine ice) and larger crystals (more aggregation, also riming).

For HAIC-HIWC data, coefficients α are retrieved, while matching measured IWC from IKP-2 with calculated IWC thereby integrating PSD times m(D) power law relationship. For MT data, coefficients α are retrieved from T-matrix simulations of the reflectivity factor (Fontaine et al., 2017). α calculation is solely constrained by the fact that the mass of ice crystals remains smaller or equal than the mass of an ice sphere with the same diameter D_{max}:

$$\alpha = \frac{CWC}{\sum_{15}^{12845} N(D_{max}) \cdot D_{max}^{\beta} \cdot \Delta D_{max}} \quad | \quad \alpha \cdot D_{max}^{\beta} \leq 0.917 \cdot \frac{\pi}{6} \cdot D_{max}^{3} \quad \left[g\ cm^{-\beta}\right]. \tag{8}$$

For the uncertainty calculation of α we take the maximum value of β which is 3:

$$\frac{U(\alpha)}{\alpha} = \sqrt{\left(\frac{U(CWC)}{CWC}\right)^2 + 3 \cdot \left(\frac{U(D)}{D}\right)^2 \left(\frac{U(N)}{N}\right)^2} \tag{9}$$

Figure 12 (a) shows median α coefficients as a function of T and MCS reflectivity zone. As has been already stated in previous studies, α is strongly linked to the variability of β (Fontaine et al., 2014; Heymsfield et al., 2010). Figure 12 (a) compared to Figure 11 (a) confirms that results for α have similar trends as those discussed for β. α vary from 5.10^{-4} (in MCS reflectivity zone 2) to ≈2.10^{-2} (in MCS reflectivity zone 8). In general, α increases as a function of T for a given MCS reflectivity zone and also increases as a function of MCS reflectivity zone (and associated IWC) for a given T level. As already stated for the median exponent β in Figure 11 (a), median α in MCS reflectivity zones 4, 5, 6, 7 and 8 are more or less overlapping. Median α in MCS reflectivity zones 2 and 3 are shown for completeness reasons, however with less confidence as they are related to IWC generally smaller than 0.1g m^{-3}.

https://doi.org/10.5194/acp-2019-502
Preprint. Discussion started: 21 June 2019
© Author(s) 2019. CC BY 4.0 License.

Atmospheric Chemistry and Physics Discussions

From Figure 12(b) and Figure 12(c) we can note, that even with a good accuracy of the measured IWC (from IKP-2; $U(IWC)/IWC \approx \pm 5\%$ for the typical IWC values observed in HAIC-HIWC at 210K), the uncertainty of α, is rather large which is mainly due to uncertainties in OAP size and concentration measurements. Taking into account the large uncertainty on the retrieved α, we find that MRD-α for all 4 tropical datasets for MCS reflectivity zones 4, 5, 6, 7, and 8 are smaller than $U(\alpha)/\alpha$. For data from Niamey (Figure 12 (e)), α tend to be larger than median α for the tropical dataset (MRD-α not centered on 0, but shifted to positive values).

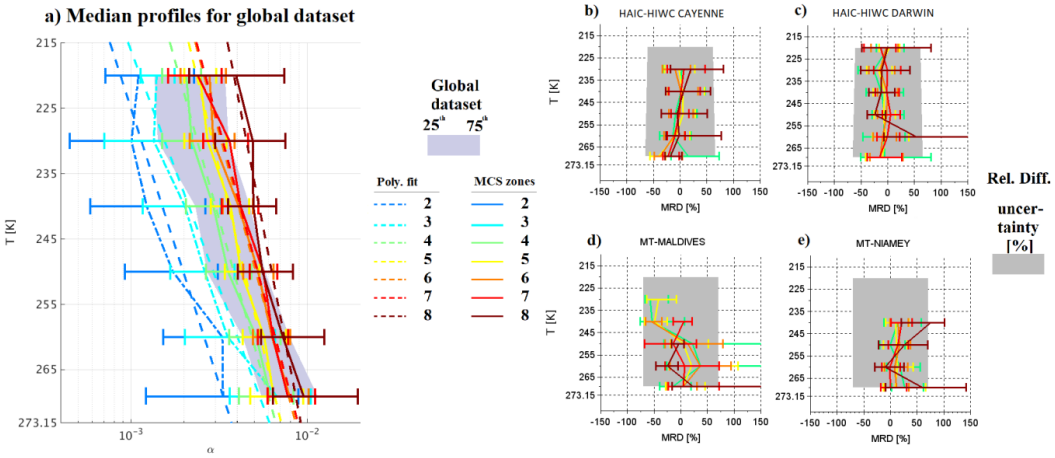

Figure 12: As Figure 5, but for pre-factor α of mass-size relationships for used ice hydrometeor size definition D_{max}.

In previous sections, this study documented similar IWC values and visible extinction coefficients for a given range of Z and T and a clear increase of IWC and visible extinction coefficient from MCS reflectivity zones 4 to 8. The increase of α and β with MCS reflectivity zones is not clearly visible, whereas at least α seems to increase with temperature in different MCS reflectivity zones). Hence, the increase of IWC, visible extinction with reflectivity zone Z is not linked to an increase of the mass-size coefficients. This conclusion takes into account the variability of the mass-size coefficients shown by 25 and 75 percentiles. However, we cannot ignore that α and β tend to be larger in MCS reflectivity zone 8 than in MCS reflectivity zone 4, especially at higher altitude.

As visible extinction (hence projected surface) and IWC are similar for the same range of T and Z in all types of MCS, we speculate that fractal dimension (hence shape) of crystals might be different from one to another MCS location. Our assumptions is that the ratio of projected surface vs IWC is similar, in other words the density of ice per surface unity (or by pixels of projected surface) is similar as function of T and Z in all types of MCS even if there might be a possibility that the habit or the shape can be different (pure oceanic MCS vs pure continental MCS).

5.5 Largest ice hydrometeors

Figure 13 investigates the variability of the size of the largest ice hydrometeors in the PSD (hereafter $max(D_{max})$ as defined in Fontaine et al (2017)). Figure 13 (a) reveals globally for all MCS reflectivity zones that the median of $max(D_{max})$ increases with T, with larger hydrometeors at cloud base compared to cloud top, particularly in the stratiform cloud part, where PSD are mainly impacted by a combination of aggregation and sedimentation. At higher levels for $T \in$ [215K; 245K[largest median of $max(D_{max})$ are observed in the most convective MCS reflectivity zone 8, followed by zones 7, 6, and 5, where sedimentation becomes more and more active. Below the 250K level, largest $max(D_{max})$ can be observed in MCS reflectivity zones 6 and 7 (still significant sedimentation source from above), followed by 5 (increasing depletion of large crystals) and 8 (more

https://doi.org/10.5194/acp-2019-502
Preprint. Discussion started: 21 June 2019
© Author(s) 2019. CC BY 4.0 License.

Atmospheric Chemistry and Physics Discussions

convective or at least transition zone from convective to stratiform cloud part). Smallest *max(D_{max})* are observed in MCS reflectivity zones 2 and 3.

MRD-*max(D_{max})* shown in Figure 13(b), 13(c), 13(d), and 13(e) are a bit larger than the measurement uncertainty estimated with ±20% ((Baumgardner et al., 2017). Cayenne, Darwin, and Niamey data are centered around the median *max(D_{max})* of the 4 tropical datasets in MCS reflectivity zone 8 for all type of MCSs, in MCSs reflectivity zone 7 in MCS over Darwin, Cayenne and Niamey. MCSs over Cayenne et Darwin tend to have similar *max(D_{max})* in other MCS reflectivity zones. Maldives dataset shows mainly negative MRD-*max(D_{max})* values, indicating that *max(D_{max})* for the Maldives Island data are generally smaller than those of the other three tropical datasets. Also MCS over Niamey show larger *max(D_{max})* in MCS reflectivity zones 2 to 4, illustrating that snow aggregates can reach larger sizes during the West African monsoon than in other MCS locations.

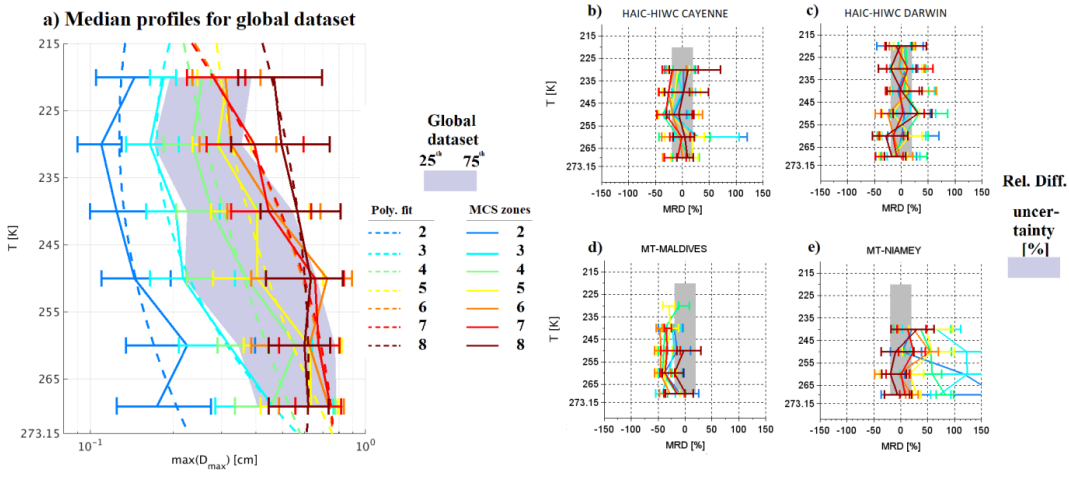

Figure 13: As Figure 5, but for maximum size of hydrometeors *max(D_{max})* in PSD in [cm].

In this section, it is shown that in the stratiform or decaying part of MCS, largest size of hydrometeors are larger in MCSs over Niamey than in other types of MCS, and that crystal aggregates tend to be smaller in MCS over Maldives Islands. Suggesting that aggregation efficiency is different from one MCS type of MCS to another, this could explain the differences of mass-size coefficient *β*, as it is calculated on the slope in a log-log scale of mean perimeter and mean surface as a function of median diameter in each size bin. Hence, large hydrometeors have a non-negligible impact on the slope (i.e. *fp* and *fs*, see Eq. (7)).

5.6 2nd and 3rd moment of PSD

5.6.1 Observations

Moments of PSD are convenient for numerical weather prediction to model microphysics of hydrometeor populations, since knowing the PSD nth order moment allows to roughly describe cloud processes and their hydrometeors properties. Commonly, number PSD of ice hydrometeors are modeled with Gamma distributions. The calculation of the n^{th} order moment is defined in Eq. (10) for PSD obtained from size distribution measurements of hydrometeors, for example with OAP (optical array probes):

$$M_n = \sum_{D_{max}=55\mu m}^{D_{max}=1{,}2cm} N(D_{max}) \cdot D_{max}^n \cdot \Delta D_{max} \quad (10)$$

The uncertainty of the nth (n=2 and 3 in our study) moment is:

https://doi.org/10.5194/acp-2019-502
Preprint. Discussion started: 21 June 2019
© Author(s) 2019. CC BY 4.0 License.

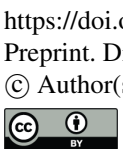

Atmospheric Chemistry and Physics Discussions

$$\frac{U(M_n)}{M_n} = \sqrt{n \cdot \frac{U(D)^2}{D} + \frac{U(N)^2}{N}} \tag{11}$$

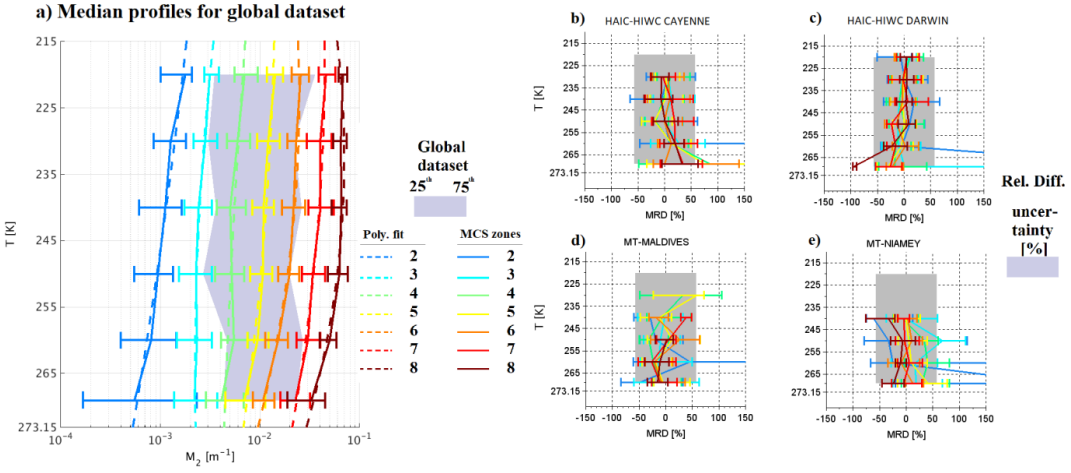

Figure 14: Same as Figure 5, but for M_2 per for unity dimension.

Figure 14 (a) shows median second moment M_2 as a function of T for all MCS reflectivity zones for the merged global tropical dataset. Median M_2 slightly decrease with temperature for all individual MCS reflectivity zones, and distinctly increase with MCS reflectivity zone for a given T. The range of variability of median M_2 shows mainly negligible overlap, if any, of 25th and 75th percentiles of neighboring MCS reflectivity zones with the exception between MCS reflectivity zones 8 and 7 at low altitude ($T \in [265; 273.15[$). All 4 tropical MCS (Figure 14 (b), (c), (d), and (e)) show good agreement with the medians of M_2 in MCS reflectivity zones 3 to 8, with MRD-M_2 significantly smaller than $U(M_2)/M_2$. Few minor exceptions can be found for MCS over Cayenne (Figure 14 (b)) and Darwin (Figure 14 (c)) in the temperature range [265K; 273.15[. Also MCS over Niamey (Figure 14 (e)) show a larger MRD-M_2 in MCS reflectivity zones 2 and 3 for $T \in$ [265K; 273.15K[and $T \in$ [245K; 255K[, respectively.

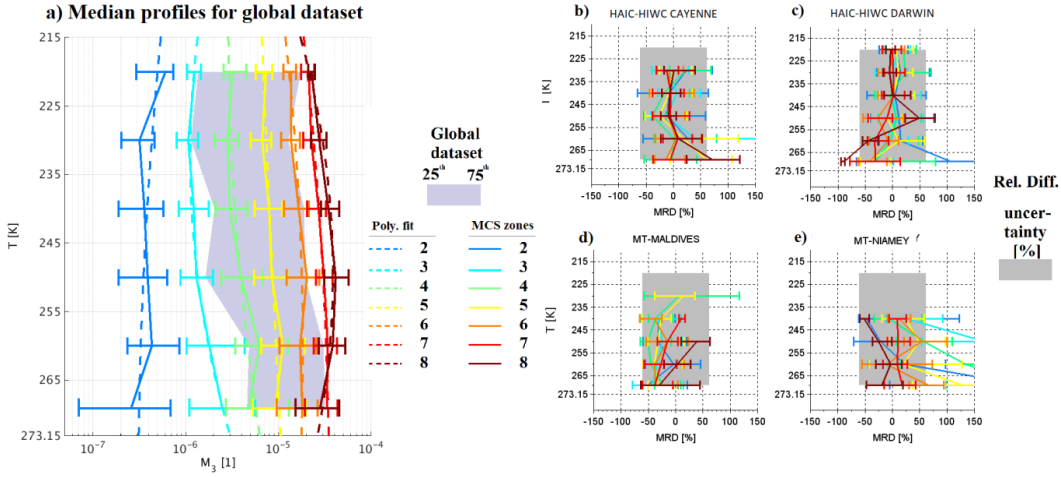

Figure 15: Same as Figure 5, but for the M_3 for unity dimension.

https://doi.org/10.5194/acp-2019-502
Preprint. Discussion started: 21 June 2019
© Author(s) 2019. CC BY 4.0 License.

Atmospheric Chemistry and Physics Discussions

Figure 15 (a)) presents median third moment M_3 for global tropical dataset as a function of T and for different MCS reflectivity zones. Median M_3 in highest MCS reflectivity zones 8, 7, and to some extent zone 6 resemble the corresponding curves of median IWC (Figure 5(a)), with a maximum value for median M_3 for $T \in$ [245K; 260K[. We also obtain a clear increase in median M_3 with MCS reflectivity zone from 2 to 8. The range of variability for M_3 reveals no overlap of 25th and 75th percentiles of neighboring MCS reflectivity zones 2-7, solely zone 7 overlaps with zone 8 for all temperatures. Third moment of MCS over Cayenne, Darwin and Maldives Islands in MCS reflectivity zones 2 to 8, shows MRD-M_3 smaller than $U(M_3)/M_3$, with few minor exceptions basically in the range of $T \in$ [265K; 273.15K[. MCS over Niamey tend to have MRD-M_3 that are sometimes larger than $U(M_3)/M_3$. Indeed, M_3 for MCS over Niamey tend to be larger in MCS reflectivity zones 5 and 2 in the range of $T \in$ [265K; 273.15K[, and in MCS reflectivity zone 4 for T larger than 255K as well as in MCS reflectivity zone 3 for T larger than 245K.

Overall, this section illustrates that second and third moments of PSD are similar as a function of T and Z for all MCS locations of the underlying dataset. However, there are exceptions in MCS reflectivity zones 2, 3 and 4 in MCS over Niamey where larger third moments are calculated compared to those deduced for the merged global tropical dataset. Despite those exceptions, the next section explores the possibility to parameterize the second and third PSD moments as a function of IWC and temperature.

5.6.2 Parameterizations

This section presents parametrizations to predict the 2nd and 3rd moment of the PSD for the global tropical dataset as a function of T and IWC, including IWC data larger than 0.1g m^{-3}. Indeed some moments can be directly linked to bulk properties of hydrometeor populations. For example, moment M_0 for ice and liquid hydrometeors is equal to the total number concentration (N_T), moments M_2 and M_3 for liquid particles are proportional to visible extinction and liquid water content. However, for ice hydrometeors the physical interpretation of moments M_2 and M_3 is less evident since ice hydrometeors are not spherical particles. The results for α and β coefficients of the m(D_{max}) relationship presented in section 5.3, illustrate that β varies between 1.5 and 2.3. This means that IWC is proportional to PSD moments between $M_{1.5}$ and $M_{2.3}$. Also uncertainties on the retrieved β coefficients do not allow to assess the variability of β as a function of IWC and T. Former studies performed in different cloud environments report mean values of β around 2. For example, Leroy et al., (2016) found β=2.15 for HAIC-HIWC in Darwin, Cotton et al., (2013) suggested β=2.0, Heymsfield et al., (2010) suggested β=2.1, and Brown and Francis (1995) established β=1.9. We are also aware of the fact that findings of β also depend on the utilized size parameter (D_{max}, D_{eq}, etc…) of 2D images. Hence, we apply β=2 as an approximation, also proposed by Field et al., (2007), to link the second moment of hydrometeor PSD with IWC (Eq. 12). Subsequently the ratio IWC/M_2 is calculated and denoted A.

$$M_2 = \frac{0.001 \cdot IWC}{A} \quad (12)$$

https://doi.org/10.5194/acp-2019-502
Preprint. Discussion started: 21 June 2019
© Author(s) 2019. CC BY 4.0 License.

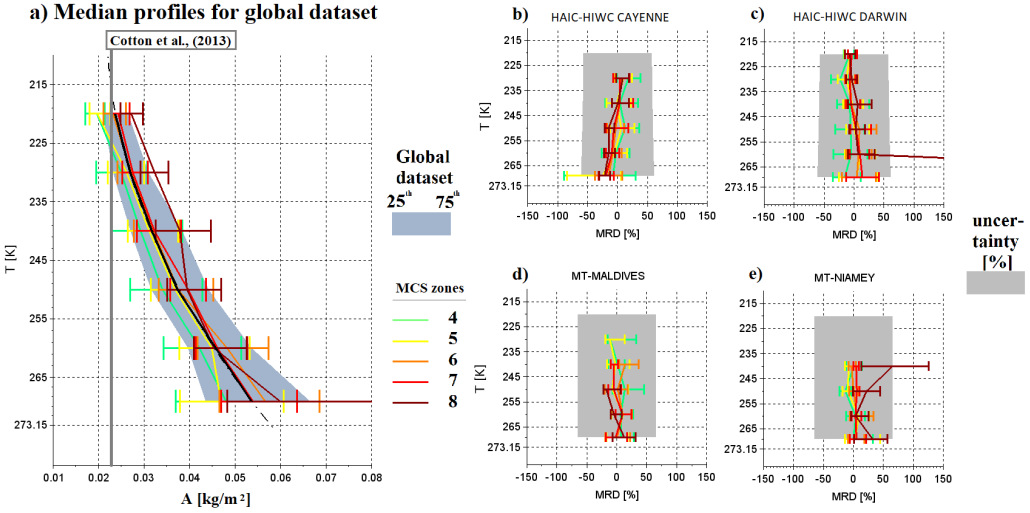

Figure 16: Same as Figure 5, but for the ratio $A = 0.001*IWC/M_2$ in [kg m^{-2}].

Figure 16 (a) shows retrieved median coefficients *A* for the global tropical dataset as a function of MCS reflectivity zone and *T*. Note that *A* is calculated in SI units (note that in Eq. (12) IWC is in g m^{-3}). The black solid line gives the median of *A* as a function of T, thereby merging all MCS reflectivity zones and all tropical datasets with IWC > 0.1g m^{-3}. The grey band gives corresponding 25th and 75th percentiles of that median *A*. In addition, are calculated median A for all individual MCS reflectivity zones (on Figure 16(a)) are solely illustrated median *A* for zones 4 to 8) for the global tropical dataset as a function of *T*. In general, median *A* calculated for individual MCS reflectivity zones 5, 6 and 7 are very similar to the median *A* when merging all MCS reflectivity zones (black solid line), whereas median *A* calculated for MCS reflectivity zone 4 tends to have smaller *A* values and median *A* calculated for MCS reflectivity zone 8 have larger median *A* values than the overall median *A* (all MCS reflectivity zones merged) for comparable temperatures.

However, when taking into account the variability in median *A* calculated for individual MCS reflectivity zones and associated 25th and 75th percentiles we can state that median *A* generally increases with *T*, however it is not possible to assess that *A* increases with MCS reflectivity zones or IWC. As a comparison, we include the value of the pre-factor α (in SI unity) from Cotton et al. (2013) mass-size relationship (β=2.0, as is for second moment M_2, and α=0.0257). Clearly, α=0.0257 is not suited for deep convective systems as it represents ice crystals for T ∈[215K; 225K[. Figure 16 (b), 16(c), 16(d), and 16(e) illustrate that MRD-*A* are significantly smaller than *U(A)/A*, (same uncertainty than α: $U(\alpha)/\alpha = U(A)/A$ and median MRD results centered around 0%). Comparing results of *A* (Figure 16, this section 5.6.2) with results presented for α (Figure 12, section 5.4) it is obvious in terms of variability and MRD in each type of MCS that *A* is better adapted to parametrize the PSD 2nd moment as a function of *T*. Eq. (13) then fits the median of ratio *A* for the global tropical dataset (black line, all MCS reflectivity zones merged), as a function of *T* in deep convective systems for IWC larger 0.1g m^{-3}:

$$A(T) = 0.0000075 \cdot T^2 - 0.0030598 \cdot T + 0.3334963 \quad (13)$$

Hence, M_3 can be deduced from M_2 and *T* from equations given by Field et al., (2007). These equations are recalled here with:

$$M_n = M_2^{F(n)} \cdot D(n) \cdot \exp(E(n) \cdot T_c) \quad (14)$$

T_C denotes temperature in °C and D(n), E(n) and F(n) are given by:

$$D(n) = \exp(13.6 - 7.76 \cdot n + 0.479 \cdot n^2) \quad (15)$$

$$E(n) = -0.0361 + 0.0151 \cdot n + 0.00149 \cdot n^2 \quad (16)$$

https://doi.org/10.5194/acp-2019-502
Preprint. Discussion started: 21 June 2019
© Author(s) 2019. CC BY 4.0 License.

Atmospheric Chemistry and Physics Discussions

$$F(n) = 0.807 + 0.00581 \cdot n + 0.0457 \cdot n^2 \quad (17)$$

Figure 17 provides median relative errors (whiskers represent 25th and 75th percentiles) of parametrized moments M_2 and M_3 compared to respective moments calculated directly (Eq. (10) from PSD measurements (global tropical dataset). These relative errors are shown as a function of IWC (Figure 17(a)) and as a function of T (Figure 17(b)). Firstly, the dashed black line shows relative error of M_2 retrieved from Eq. (12+13) compared to M_2 derived from measured PSD (Eq. 10). In addition the grey band illustrates the uncertainty $U(M_2)/M_2$. Figure 17 (a) illustrates that below 2g m^{-3}, the median of this relative error is close to 0% with 25th and 75th percentiles significantly smaller than $U(M_2)/M_2$. However, for largest IWC beyond 2g m^{-3}, median relative errors are getting large (40% for 4g m^{-3} and 75% for 4.5g m^{-3}) and need to be corrected in order to reduce the bias between predicted M_2 and observed M_2. This is why Eq. (12) has been modified with an expression shown in Eq. (18) in order to improve prediction of M_2 compared to measured M_2 (Eq. (10)) for highest IWC:

$$M_2 = \frac{0.001 \cdot IWC}{A(T)} \cdot [-0.0074517 \cdot exp(IWC) + 1.0246154] \quad (18)$$

The effect of the expression added in Eq. (18) is illustrated by the solid black line in Figure 17 (a), where median relative error of predicted M_2 is now closer to 0% also for large IWC. Still, Eq. (18+13) seems to underestimate measured M_2 by about 15% for IWC of 4.5g m^{-3} instead of 75% overestimation before correction. Note that in Figure 17 (b), median relative errors of the two above parametrizations (black dashed and black solid line) of M_2 are superposed as a function of T with a median relative error close to 0%. This means that the second part of equation (18) does not introduce any significant bias as a function of T, since the occurrence of IWC > 2g m^{-3} is smaller than 1% for the global tropical dataset.

Secondly, two types of parametrized third moments (using parametrization of 3rd moment M_3 (Eq. (14) according to Field et al., (2007) that can be deduced from 2nd moment M_2 and T) are calculated and subsequently compared with the third moment derived from measured PSD (Eq. (10)). The first type of parametrized M_3 (red lines in Figure 17) is derived from measured M_2 moments (Eq. (10)) and the second type of M_3 (blue lines in Figure 17) from parametrized M_2 moments (Eq. (12+13)). For the latter case we voluntarily did not choose Eq. (18+13) but stayed with Eq. (12+13).

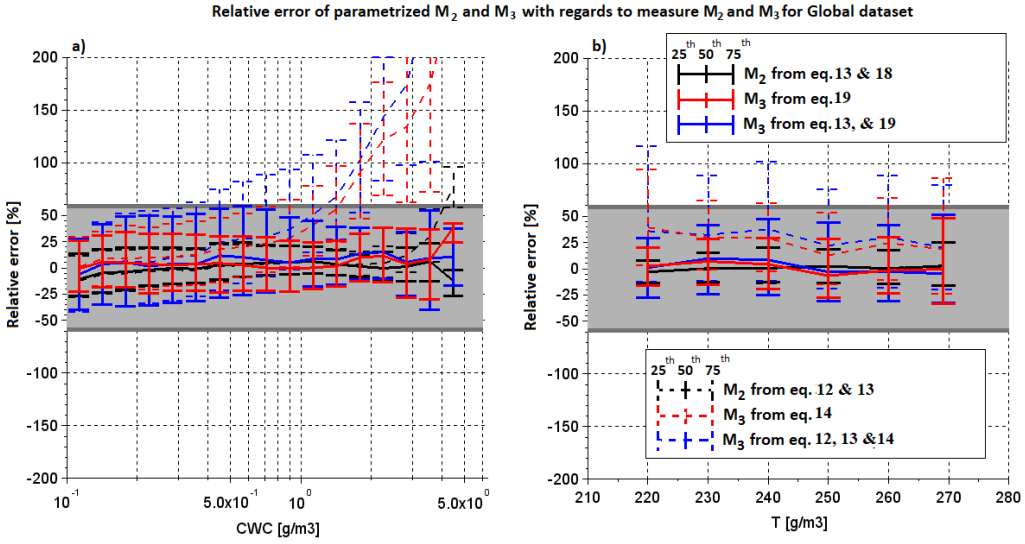

Figure 17: Relative error of parametrized M_2 and M_3 for global tropical dataset as a function of IWC in a) and as a function of T in b). Solid lines give median relative error and whiskers denote 25th and 75th percentiles of relative error. Grey bands and dark grey lines shows measurement uncertainties for M_2 (55%) and M_3 (61%), respectively.

https://doi.org/10.5194/acp-2019-502
Preprint. Discussion started: 21 June 2019
© Author(s) 2019. CC BY 4.0 License.

Atmospheric Chemistry and Physics Discussions

Red dashed lines in Figure 17 show median relative error with 25th and 75th percentiles when M_3 are calculated from measured M_2 and Eq. (14) and blue dashed lines represent median relative error with 25th and 75th percentiles when M_3 is calculated from parametrized M_2 from Eq. (12+13) and Eq. (14). Figure 17 (b) demonstrates that M_3 in deep convective systems calculated from M_2 with Eq. (14) have a positive median relative error of about +25%, which is true for both type of M_2 calculations (measurement, parametrization) inserted in Eq. (14). Moreover, median relative error of M_3 generally increase with IWC from 0% at 0.2g m^{-3} to more than 200% at 3g m^{-3}. Thus, not applying the M_2 correction for highest IWC (Eq. 18), we also show that produced M_3 moments from parametrized M_2 moments are slightly worse than M_3 moments produced from measured M_2 moments. To reduce this significant median relative error in M_3, particularly for large IWC in deep convective cloud systems, we provide an M_3 correction function for Eq. (14) depending on T and IWC:

$$M_3 = [0.0001713 \cdot T \cdot IWC^2 - 0.0013992 \cdot T \cdot IWC + 0.0045791 \cdot T + 0.0032021 \cdot IWC - 0.0807616] \cdot M_2^{F(3)} \cdot D(3) \cdot \exp(E(3) \cdot T_c) \quad (19)$$

Two series of median relative error for M_3 estimated from Eq. (19) and compared to M_3 calculated directly from PSD measurements (Eq. (10)) are plotted in red and blue solid lines with 25th and 75th percentiles in Figure 17. Red solid lines represent median relative error when estimated M_3 are calculated from measured M_2 and Eq. (19) and blue solid lines represent median relative error when estimated M_3 is calculated from parametrized M_2 from Eq. (18+13) and Eq. (19). Median relative errors are similar for both type of predictions of M_3 and close to 0%, but for the predicted M_3 using Eq. (18) and Eq. (19) the absolute values of 25th or 75th percentiles are larger than for M_3 predicted from observed M_2 and Eq. (19), showing that prediction of M_2 and M_3 increase the deviation around median measured M_3.

An identical investigation on median relative errors in the prediction of 2nd and 3rd moment as presented in Figure 17 has been investigated for individual MCS locations (figures not shown). For all type of tropical MCS, we observe that M_2 from Eq. (18) and M_3 from Eq. (19) tend to have smaller to equal median relative errors compared to the relative uncertainties $U(M_2)/M_2$ and $U(M_3)/M_3$, respectively. Beyond this general statement there are two noticeable observations. The first observation is that median relative errors of M_3 from Eq. (19) calculated either with M_2 from measurements (Eq. (10)) of from parametrized M_2 from Eq. (18) for MCS over Maldives Islands are close to $U(M_3)/M_3$ with 75th percentiles reaching 100% for IWC in the [0.3; 0.6] g m^{-3}. The second observation is that for MCS over Niamey, M_3 from Eq. (19) with M_2 from Eq. (10) or from Eq. (18) tend to overestimate respective moments calculated directly from PSD measurements by about 30 or 50%, respectively, in the area of higher IWC ([2; 3] g m^{-3}).

This section aims to produce parameterizations of the second and third moments of ice hydrometeor size distributions, which can be useful for the calculation of hydrometeor size distributions in numerical weather prediction using gamma distributions, but also (see the next section) for calculating rescaled ice hydrometeors size distributions (Field et al., 2007).

5.6.3 Rescaling of measured PSD

From bulk properties as mixing ratio and total concentration in numerical weather prediction (NWP), ice hydrometeors size distributions (or PSD) properties can be derived from moment parameterization allowing simplified prediction of cloud microphysical processes such as precipitation. Usually, ice hydrometeors size distributions for hydrometeors are modeled by gamma distributions. Since the method of gamma distributions is relatively well documented, we focus this study on another type of PSD parameterization, which studies 'rescaled PSD' dealing with a 'mean diameter' defined by the ratio of the third moment over the second moment.

In this section, we propose an update for the method proposed by Field et al., (2007) for deep convective cloud systems and IWC larger than 0.1g m^{-3}. For the entire dataset of this study we therefore apply the above method utilizing Eq. (20) and Eq. (21) to calculate function $\Phi_{2,3}$(x) and x for individual measured PSD :

$$\Phi_{2,3}(x) = N(D_{max}) \cdot \frac{M_3^3}{M_2^4} \quad (20)$$

https://doi.org/10.5194/acp-2019-502
Preprint. Discussion started: 21 June 2019
© Author(s) 2019. CC BY 4.0 License.

Atmospheric Chemistry and Physics Discussions

With x being the characteristic size:

$$x = D_{max} \cdot \frac{M_2}{M_3} = \frac{D_{max}}{L_{2,3}} \quad (21)$$

$\Phi_{2,3}(x)$ and x are dimensionless functions. Moreover, Field et al., (2007) deduced from their dataset, $\Phi_{2,3}(x)$ depending on cloud location; i.e. tropical troposphere or mid-latitude troposphere (here we focus on the equation established for the tropics):

$$Tropics: \Phi_{2,3}(x) = 152 \cdot \exp(-12.4 \cdot x) + 3.28 \cdot x^{-0.78} \cdot \exp(-1.94 \cdot x) \quad (22)$$

Hence, the variability of PSD in clouds, is not given by $\Phi_{2,3}(x)$ but by the variability of the 2nd and 3rd moments that allow retrieving functions x and $\Phi_{2,3}(x)$. Then, knowing $x, \Phi_{2,3}(x)$, M_2, and M_3 concentrations of ice hydrometeors can be parameterized such:

$$D_{max} = x \cdot \frac{M_3}{M_2} \quad (23)$$

And

$$N(D_{max}) = \Phi_{2,3}(x) \cdot \frac{M_2^4}{M_3^3} \quad (24)$$

Figure 18 shows the probability distribution function (PDF) of observed rescaled PSD in tropical MCS as a function of the x parameter. Thick black line represents $\Phi_{2,3}(x)$ from Field et al., (2007), thin dashed grey line represents median of $\Phi_{2,3}(x)$ for a given range of x, with whiskers showing 25th and 75th percentiles of $\Phi_{2,3}(x)$. The figure illustrates that Eq. (22) from Field et al., (2007) represents rather well $\Phi_{2,3}(x)$ as a function of x in highest PDF region (dark red area) and fits well the median plot for $x \in [0.3; 6]$. However, Field et al., (2007) performed their study for diameter larger than 100µm while this study calculates rescaled PSD for D_{max} larger than 15µm for the underlying dataset. Thus, Eq. (22) does not fit median $\Phi_{2,3}(x)$ for x smaller than 0.3. Also for $x > 6$, Eq. (22) decreases too fast compared to the median of $\Phi_{2,3}(x)$ calculated for the global tropical dataset of this study, although Field et al., (2007) considered ice hydrometeors up to 20000µm, whilst this study extrapolates PSD until 12845µm only. A likely assumption to explain the differences for large $x > 6$ might be that the global tropical dataset of this study may have measured PSD with largest hydrometeors at a far higher frequency than this was the case for the dataset of Field et al., (2007).

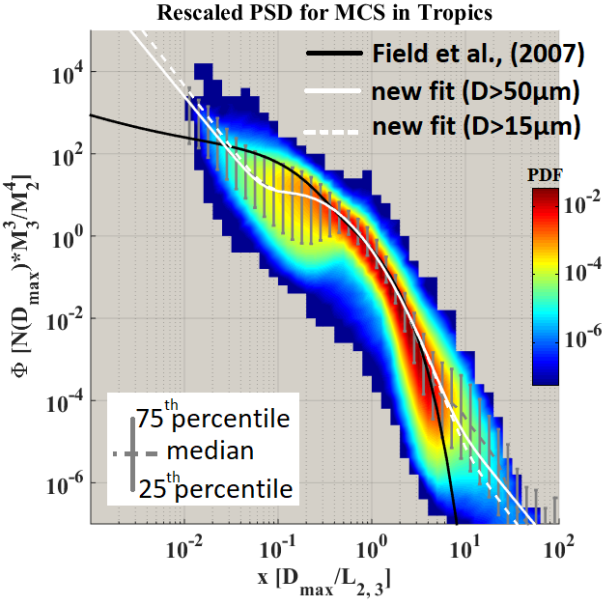

https://doi.org/10.5194/acp-2019-502
Preprint. Discussion started: 21 June 2019
© Author(s) 2019. CC BY 4.0 License.

Atmospheric Chemistry and Physics Discussions

Figure 18: Probability distribution function of rescaled PSD ($\Phi_{2,3}$) on y axis as a function of hydrometeor characteristics size (x) on x axis, for the Global tropical datasets. Black lines show fitted functions from Field et al., (2007), grey dotted lines show median rescaled PSD with error bar from 25th and 75th percentiles of rescaled PSD. Solid white line presents the new fitted function for the global tropical dataset for PSD beyond 55µm and dashed white line shows fitted function for PSD beyond 15µm (Eq. 25).

White lines (dashed and solid) show new fitted $\Phi_{2,3}(x)$ for the global tropical dataset of this study. The white dashed and solid lines can be represented by the following equation and aim to fit the median ($\Phi_{2,3}(x)$) of Figure 19(a) as a function of x:

$$Tropics: \Phi_{2,3}(x) = [\exp(a_1) \cdot x^{a_2}] + \left[b_1 \cdot exp\left(-\frac{(\ln(x) - b_2)^2}{b_3^2}\right)\right] \quad (25)$$

Where b1 = 9.484, b2 = -1.895 and b3 = 1.083. Note that dashed and solid white lines use different sets of coefficients a_1 and a_2 (Table 1). For white dashed line, a_1 and a_2 are calculated for D_{max} beyond 15µm, whereas for white solid line, a_1 and a_2 are calculated for D_{max} beyond 55µm. We can notice that the function for $D_{max} \geq$ 15µm produces higher $\Phi_{2,3}(x)$ as compared to the function fitted for $D_{max} \geq$55µm. In order to explain this difference, we recall that for MCSs over the Maldives Island concentrations of hydrometeors with $D_{max} \leq$55µm are higher compared to 3 other tropical MCS locations, which could affect the fitted coefficients a_1 and a_2 in the two different versions of $\Phi_{2,3}(x)$ calculations for the global tropical dataset. Another difference in small particle measurements could be a pure technical difference in small particle measurements (including shattering/out-of-focus/small sample volume artefacts) between 2D-S probe (this study) and 2D-C probe (Field et al. (2007) study).

Table 1 : Coefficients a1 and a2 for Eq. (25).

	a_1	a_2
Tropics: D_{max} >15µm	-5.4114	-3.0026
Tropics: D_{max} > 55µm	-5.0032	-2.7822

6 Discussion and conclusion

In this study we analyze in-situ aircraft observations of the ice particle size distributions and simultaneous cloud radar observations collected in tropical MCS in order to characterize the statistical properties of ice microphysics. The results are focused on the tropical MCS that include observations from: (i) the raining season over Cayenne (South America), (ii) the North-Australian monsoon over Darwin, (iii) deep convective systems over the Maldives Island in the ITCZ, and (iv) the West-African monsoon over Niamey.

The overall data analysis of ice hydrometeor properties has been performed as a function of temperature and the range of radar reflectivity factors measured at 94GHz. Therefore, all vertical profiles of aircraft onboard radar reflectivity measurements have been gathered and statistically analyzed in order to define delimited reflectivity zones, thereby reducing possible vertical bias due to the chosen flight track/altitude in the MCS systems. Hence, this study defines 8 MCS reflectivity zones that have been determined from radar reflectivity factor percentiles (1st 10th 30th 50th 70th 90th and 99th) as a function of temperature, thereby merging all vertical reflectivity profiles of the entire global tropical dataset used for this study. Analysis of the retrieved vertical wind speeds in each MCS reflectivity zone reveals that the probability to observe a magnitude of vertical winds larger than 1m.s^{-1} are not that different in MCS reflectivity zones 1 to 5, but then strongly increase from MCS reflectivity zone 6 to 8. Generally, these probabilities increase with decreasing temperature for all MCS reflectivity zones. Also, the simple magnitude of vertical wind speeds is larger in MCS reflectivity zones 7 and 8, while in MCS reflectivity zones 1 to 6 the magnitude is rather small and similar, however the magnitude is a function of T. From this, the study demonstrates that MCS reflectivity zones 7 and 8 exhibit highest probability to be related to the active convective zone and/or the most turbulent transition zone between the inaccessible part of the convective core and the stratiform part of MCS clouds, whereas MCS reflectivity zones 1 to 5 are rather associated with the decaying or so-called stratiform parts of MCS. MCS reflectivity zone 6 then represents the

https://doi.org/10.5194/acp-2019-502
Preprint. Discussion started: 21 June 2019
© Author(s) 2019. CC BY 4.0 License.

Atmospheric Chemistry and Physics Discussions

transition between stratiform and convective area of an MCS with a relatively small median magnitude of vertical winds, however with relatively high probability of vertical wind magnitudes beyond 1m s^{-1}.

Subsequently, the study compares microphysical properties (such as ice water content, extinction, concentrations, largest hydrometeor sizes, etc…) as a function of MCS reflectivity zone and temperature. The statistical analysis (median values, 25th and 75th percentiles) is performed for individual the MCS locations), whereas the merged dataset of the 4 tropical MCS locations serves as a reference. Relative differences of median microphysical properties in one MCS location compared to respective median properties of the reference dataset were quantified. Also uncertainties for all type of microphysical measurements and retrieved cloud parameters were calculated from Baumgardner et al. (2017).

Table 2 summarizes qualitatively the findings for IWC, visible extinction (σ), total concentrations ($N_{T,50}$ for D_{max}>50µm; $N_{T,500}$ for D_{max}>500µm), 2nd moment (M_2) and 3rd moment (M_3) of hydrometeor PSD, and largest hydrometeors sizes ($max(D_{max})$). Within the range of uncertainties, we showed that the variability of IWC, σ, $N_{T,50}$, $N_{T,500}$, M_2 and M_3 as a function of temperature and specific MCS reflectivity zones tends to be similar: For example, for IWC these conclusions apply for MCS reflectivity zones 4 to 8. MCS data from Niamey flight campaign (compared to the three other tropical MCS locations) reveal more exceptions when compared with median parameters calculated for the global tropical dataset, with a trend of larger 3rd PSD moments and larger hydrometeor sizes in the stratiform area of MCS. Assuming that largest hydrometeors ($max(D_{max})$) can be considered as a proxy for the aggregation process efficiency, findings of this study reveal that $max(D_{max})$ are similar in MCSs over Darwin and Cayenne (as a function of T and Z), but different for MCS over Niamey and Maldives Islands. Indeed, MCS over Niamey have larger $max(D_{max})$, whereas MCS over Maldives Islands shows smaller $max(D_{max})$ than MCS over Cayenne and Darwin. Hence, the aggregation process is more efficient in MCS over Niamey during the West-African Monsoon than for the other type of tropical MCS and less efficient in MCS over Maldives Islands.

Table 2: Evaluation of parameter X (X for IWC, σ, $N_{T,55}$, $N_{T,500}$, , M_2, M_3 and $max(D_{max})$) , for each type of tropical MCS (Darwin, Cayenne, Maldives Islands, Niamey) with respect to the global tropical dataset thereby comparing median values in corresponding MCS reflectivity zones. Two sub-columns for each type of MCS: The first column gives an evaluation of the main trend: ≅ if MRD-X is comparable to the uncertainty range, + if MRD-X is larger than the uncertainty range, - for smaller values. In the second sub-column are reported the number of exceptions with respect to the main trend (first column) with: Z(Y)≅ or Z(Y)+ or Z(Y)-. Z number stands for a particular MCS reflectivity zone (with Z= 2, 3, 4, 5, 6, 7, 8) , Y number represents a particular T range (with Y=1 for T ∈ [265K; 273.15K[, Y=2 for T ∈ [255K, 265K[, Y=3 for T ∈ [245K; 255K[, Y=4 for T ∈ [235K; 245K[, Y=5 for T ∈ [225K; 235K[, and Y=6 for T ∈ [215K; 225K[).

With respect to median of	MCS over Darwin		MCS over Cayenne		Maldives Islands MCS		Niamey's MCS	
IWC	≅	4(6)+, 5(1)-	≅	4(1,5)-, 5(5)-	≅		≅	4(2)+
σ	≅	5(1)+	≅	8(1)-	≅		≅	2(4)-
$N_{T,55}$	≅	4(1)+	≅	3(1)+	≅		≅	8(3)+, 3(3)+
$N_{T,500}$	≅	8(1)+, 7(1)+	≅	8(3)+, 8(1)-	≅	7(4)+, 3(1)+	≅	8(1)-
M_2	≅	4(1)+, 5(1)+	≅	8(1)-, 2(1)+	≅		≅	4(6), 2(6)+
M_3	≅	8(1)+	≅	8(1)+, 2(1)+	≅		≅	2(1)+, 3(1,2,3)+ 4(1,2)+ 5(1)+
$max(D_{max})$	≅	2(2)+, 7(3,4)-	≅	6(3)-, 8(2)-, 8(3)+	-	8≅	+	6(1,2) ≅, 7 ≅, 8 ≅

https://doi.org/10.5194/acp-2019-502
Preprint. Discussion started: 21 June 2019
© Author(s) 2019. CC BY 4.0 License.

Atmospheric Chemistry and Physics Discussions

From the tropical dataset a parametrization of visible extinction is developed as a function of temperature and IWC (Eq. 3). This model allows retrieving σ from OAP measurements with an accuracy smaller than the measurement uncertainty of σ ($U(\sigma)/\sigma$ = 57%; Eq. (2)) for all four types of tropical MCS. Eq. (3) reveals best accuracy to represent directly calculated σ in MCS over Darwin and Niamey.

Also in this study the relationship between mass and size of ice hydrometeors ($m=\alpha.D^{\beta}$) is formulated with a classical power law approximation. A basic finding is that the variability of retrieved β throughout all MCS reflectivity zones is too large compared to its uncertainty. This would mean for example that varying β parameterization in NWP is not worthy to do. Indeed, NWP schemes are used to describe ice microphysics with PSD moments (here M_2 and M_3). Setting β=2 for the mass-size relationship allows to link IWC to the second moment directly as stated in Field et al., (2007).

Defining A as the ratio IWC/M_2, this study illustrates that A increases with temperature. Also A in MCS reflectivity zones 5, 6 and 7 are similar to the median A calculated for the entire dataset (Figure 16(a)). In MCS reflectivity zone 4 (smaller zones were not considered), A tends to be smaller in MCS reflectivity zones 4 and in MCS reflectivity zone 8, A tends to be larger than the median of A for the global tropical dataset. However, MCS reflectivity zones 4 and 8 share a wide range of variability with MCS reflectivity zones 5, 6 and 7. Hence, we use the variability of A as a function of temperature (parametrization in Eq. (13)) to predict the 2nd PSD moment in tropical and mid-latitude MCS. Whereas Eq. (13) retrieves M_2 in all type of MCS with a good accuracy, a correction is needed for high IWC (Eq. 18).

Hence, in this study the model of PSD moments presented by Field et al., (2007), has been considerably modified for PSD in deep convective cloud systems in order to predict the 3rd moment (M_3) from the known 2nd moment (M_2), IWC, and temperature T. This new parametrization of M_3 for deep convective cloud systems and IWC larger than 0.1 g m^{-3} is given by Eq. (13), Eq. (18) and Eq. (19). The prediction of M_2 (Eq. 18) is more accurate than the prediction of M_3 (Eq. 19), when compared with M_2 and M_3 directly calculated from the measured PSD. Indeed, the predicted M_2 have median relative errors in the range [-25%; 25%] (corresponds to 25th and 75th percentiles of relative error of M_2) with an uncertainty of measured M_2 of about 55%. The predicted M_3 have median relative errors in the range [-40%; 55%] (which corresponds to 25th and 75th percentiles of relative error of M_3) with an uncertainty of measured M_3 of 61%.

Furthermore, we applied on the 4 tropical datasets the method of Field et al., (2007) of PSD rescaling with 2nd and 3rd moments of the measured PSD.

Field et al., (2007) gave for their dataset a parametrized function $\Phi_{2,3}$ that models rescaled PSD in the tropics as a function of the mean diameter (ratio between the 3rd moment and the 2nd moment of the PSD). The calculated rescaled PSD for the 4 tropical datasets are in good agreement with $\Phi_{2,3}$ parametrization given by Field et al., (2007) from diameters between 0.3-6 times the mean diameter (dimensionless characteristic size x). Below, 0.3 times the mean diameter, $\Phi_{2,3}$ of Field et al., (2007) tend to overestimate the rescaled PSD and finally underestimate them again below 0.03 times the mean diameter. These differences can be explained because of different diameter threshold to calculate the rescaled PSD. In our study, we calculate rescaled PSD starting at 15µm (or 55µm; see table 1 and Eq. (25)) while Field et al., (2007) used PSD only beyond 100µm. Also for large mean diameters we note significant differences between the rescaled PSD for the dataset of this study and $\Phi_{2,3}$ parametrization from Field et al., (2007). Indeed, for diameters larger than 6 times the mean diameter, $\Phi_{2,3}$ of Field et al., (2007) decreases rapidly and therefore underestimates the rescaled PSD by about 1 order of magnitude at diameters equal to 10 times the mean diameter. We do not think that these differences are due to the difference in the cut-off diameter of PSD (last available diameter for PSD) which has been 20000µm in Field et al., (2007) against 12845µm in this study. Field et al., (2007) used PSD of ice hydrometeors measured in anvils and cirrus clouds while the entire dataset for this study has been gathered closest to MCS stratiform and convective zones of deep convective systems.

https://doi.org/10.5194/acp-2019-502
Preprint. Discussion started: 21 June 2019
© Author(s) 2019. CC BY 4.0 License.

Atmospheric Chemistry and Physics Discussions

This latter fact more likely explains differences between the rescaled PSD of this study and parametrized $\Phi_{2,3}$ from Field et al., (2007). Probably, the underlying dataset for this study contains more large hydrometeors in non-negligible concentrations, and related increased statistics on large hydrometeor concentrations.

The parametrization based on tropical PSD data beyond 15µm seems to degrade parametrization results for largest diameters (rescaled concentrations beyond parametrization). We suspect that this is due to very high concentrations of small hydrometeors in the range 15-55µm in MCS over Maldives Islands, which would finally suggest to recommend parametrization for tropical MCS solely based on PSD beyond 50µm, in order to retrieve ice properties in deep convective clouds that could serve in NWP. Moreover, findings in this study suggest to use a range of IWC and temperature T to evaluate the efficiency of NWP for deep convective systems, since this study provides a corresponding range of radar reflectivity factors, total concentrations, visible extinction, and 2nd and 3rd PSD moments. These quantities can be compared with NWP output, to target more accurately which parameters are well represented in NWP, and which are not.

Finally, several findings from this study suggest more investigations on the variability on the relationship between projected surface and mass of ice hydrometeors encountered in underlying observations. Indeed, we find that ice "density" is similar as a function of *T* and *Z* reflectivity ranges in all 4 MCS locations. Hence, this is referring to the possibility to investigate a surface-mass relationship in MCS that should be a function of *T* and *Z*. Estimating that aerosol loads and corresponding CCN and IN properties may be more or less different in these four locations (continental aerosol over Africa with a strong influence of dust from Sahara, more cleaner troposphere over the Indian ocean, merging of continental and oceanic influences), we stipulate the need of investigating secondary ice production processes, that seem to regulate the concentrations of ice hydrometeors beyond 55µm.

Author contribution

Emmanuel Fontaine, Julien Delanoë, Alfons Schwarzenboëck and Alain Protat for conceptualized this study. John Walter Strapp, Lyle Edward Lilie, Emmanuel Fontaine, Delphine Leroy, Julien Delanoë and Alain Protat for data curation of this study. John Walter Strapp, Lyle Edward Lilie, Delphine Leroy, Julien Delanoë and Emmanuel Fontaine to perform the formal analysis. Alain Protat and Fabien Dezitter for funding acquisition for campaign observations. Alfons Schwarzenboëck, Lyle Edward Lilie, John Walter Strapp, Alain Protat Delphine Leroy, Julien Delanoë and Emmanuel Fontaine for investigations performed in this study. Lyle Edward Lilie, Delphine Leroy, Julien Delanoë and Emmanuel Fontaine for developing methodology used in this study. John Walter Strapp, Fabien Dezitter and Alfons Schwarzenboëck for the project administration. Alfons Schwarzenboëck, John Walter Strapp and Julien Delanoë for providing resources. Lyle Edward Lilie, Delphine Leroy and Emmanuel Fontaine for the development of software used in this study. Alfons Schwarzenboëck for the supervision of this study. Emmanuel Fontaine to provide visualization.

Emmanuel Fontaine for writing original draft. Alfons Schwarzenboëck, Alain Protat, John Walter Strapp, Fabien Dezitter and Julien Delanoë for writing review and editing.

Data availability

The HAIC-HIWC dataset that has been used within this study is shared within the European and North American HAIC/HIWC community for analysis and completion of aircraft industry/rulemaking and science objectives. A data sharing protocol has to be agreed upon and signed by all the parties. This means that post-processed data will be available to public not before January 2021. Therefore we cannot reply positively to demands TS5 and TS11, since rulemaking is actually ongoing within FAA and EASA aviation safety agencies, thereby processing the HAIC/HIWC data set. Concerning the dataset for the campaigns of observations of the Megha-Tropiques project: optical array probes data are available by contacting Alfons Schwarzenboëck and radar data are available by contacting Julien Delanoë.

https://doi.org/10.5194/acp-2019-502
Preprint. Discussion started: 21 June 2019
© Author(s) 2019. CC BY 4.0 License.

Atmospheric Chemistry and Physics Discussions

Acknowledgements

The authors are grateful to Centre National d'Etude Spatiale (CNES) for funding the aircraft measurement campaigns within the Megha-Tropiques project. The data were collected using instruments from the French Airborne Measurement Platform, a facility partially funded by CNRS/INSU and CNES. The research leading to these results (HAIC-HIWC project) has received funding from (i) the European Union's Seventh Framework Program in research, technological development and demonstration under grant agreement no. ACP2-GA-2012-314314, (ii) the European Aviation Safety Agency (EASA) Research Program under service contract no. EASA.2013.FC27, and (iii) the Federal Aviation Administration (FAA), Aviation Research Division, and Aviation Weather Division, under agreement CON-I-1301 with the Centre National de la Recherche Scientifique. Funding to support flight project was also provided by the NASA Aviation Safety Program, the Boeing Co., and Transport Canada. Additional support was also provided by Airbus SAS Operations, Science Engineering Associates, the Bureau of Meteorology, Environment Canada, the National Research Council of Canada, and the universities of Utah and Illinois. The authors thank the SAFIRE facility for the scientific airborne operations. SAFIRE (http://www.safire.fr) is a joint facility of CNRS, Météo-France, and CNES dedicated to flying research aircraft.

References

Bailey, M.P., Hallett, J.: A Comprehensive Habit Diagram for Atmospheric Ice Crystals: Confirmation from the Laboratory, AIRS II, and Other Field Studies. J. Atmos. Sci. 66, 2888–2899. https://doi.org/10.1175/2009JAS2883.1, 2009.

Baumgardner, D., Abel, S.J., Axisa, D., Cotton, R., Crosier, J., Field, P., Gurganus, C., Heymsfield, A., Korolev, A., Krämer, M., Lawson, P., McFarquhar, G., Ulanowski, Z., Um, J.: Cloud Ice Properties: In Situ Measurement Challenges. Meteorological Monographs 58, 9.1-9.23. https://doi.org/10.1175/AMSMONOGRAPHS-D-16-0011.1, 2017.

Baumgardner, D., Brenguier, J.L., Bucholtz, A., Coe, H., DeMott, P., Garrett, T.J., Gayet, J.F., Hermann, M., Heymsfield, A., Korolev, A., Krämer, M., Petzold, A., Strapp, W., Pilewskie, P., Taylor, J., Twohy, C., Wendisch, M., Bachalo, W., Chuang, P.: Airborne instruments to measure atmospheric aerosol particles, clouds and radiation: A cook's tour of mature and emerging technology. Atmospheric Research 102, 10–29. http://dx.doi.org/10.1016/j.atmosres.2011.06.021, 2011.

Brown, P.R.A., Francis, P.N., 1995. Improved Measurements of the Ice Water Content in Cirrus Using a Total-Water Probe. Journal of Atmospheric and Oceanic Technology 12, 410–414. https://doi.org/10.1175/1520-0426(1995)012<0410:IMOTIW>2.0.CO;2, 1995.

Cetrone, J., Houze, R.A.: Anvil clouds of tropical mesoscale convective systems in monsoon regions. Quarterly Journal of the Royal Meteorological Society 135, 305–317. https://doi.org/10.1002/qj.389, 2009

Cotton, R.J., Field, P.R., Ulanowski, Z., Kaye, P.H., Hirst, E., Greenaway, R.S., Crawford, I., Crosier, J., Dorsey, J.: The effective density of small ice particles obtained from in situ aircraft observations of mid-latitude cirrus. Q.J.R. Meteorol. Soc. 139, 1923–1934. https://doi.org/10.1002/qj.2058, 2013.

Coutris, P., Leroy, D., Fontaine, E., Schwarzenboeck, A.: An Inverse Problem approach for the retrieval of ice particle mass from in-situ measurements. J. Atmos. Oceanic Technol. https://doi.org/10.1175/JTECH-D-17-0013.1, 2017

Davison, C. R., Strapp, J. W., Lilie, L., Ratvasky, T. P., and Dumont, C.: Isokinetic TWC Evaporator Probe: Calculations and Systemic Error Analysis, 2016, 8th AIAA Atmospheric and Space Environments Conference, Washington, DC. AIAA-4060. http://dx.doi.org/10.2514/6.2016-4060, June 17, 2016.

Davison, C. R., Landreville, C., and MacLeod, J. D.: Initial Development and Testing of Isokinetic Probe to Measure Total Water Content During Ground and Airborne Testing," NRC, LTR-GTL-2010-0002, Ottawa, Mar. 2010.

Field, P.R., Wood, R., Brown, P.R.A., Kaye, P.H., Hirst, E., Greenaway, R., Smith, J.A.: Ice Particle Interarrival Times Measured with a Fast FSSP. J. Atmos. Oceanic Technol. 20, 249–261. https://doi.org/10.1175/1520-0426(2003)020<0249:IPITMW>2.0.CO;2, 2003.

© Author(s) 2019. CC BY 4.0 License.

Delanoë, J., Protat, A., Bouniol, D., Heymsfield, A., Bansemer, A., Brown, P.: The Characterization of Ice Cloud Properties from Doppler Radar Measurements. J. Appl. Meteor. Climatol. 46, 1682–1698. https://doi.org/10.1175/JAM2543.1, 2007.

Delanoë, J.M.E., Heymsfield, A.J., Protat, A., Bansemer, A., Hogan, R.J.: Normalized particle size distribution for remote sensing application. Journal of Geophysical Research: Atmospheres 119, 4204–4227. https://doi.org/10.1002/2013JD020700, 2014.

Delrieu, G., Nicol, J., Yates, E., Kirstetter, P.-E., Creutin, J.-D., Anquetin, S., Obled, C., Saulnier, G.-M., Ducrocq, V., Gaume, E., Payrastre, O., Andrieu, H., Ayral, P.-A., Bouvier, C., Neppel, L., Livet, M., Lang, M., du-Châtelet, J.P., Walpersdorf, A., Wobrock, W.: The Catastrophic Flash-Flood Event of 8–9 September 2002 in the Gard Region, France: A First Case Study for the Cévennes–Vivarais Mediterranean Hydrometeorological Observatory. J. Hydrometeor 6, 34–52. https://doi.org/10.1175/JHM-400.1, 2005.

Drigeard, E., Fontaine, E., Wobrock, W., Schwarzenböck, A., Duroure, C., Williams, E.R., Russell, B., Protat, A., Delanoë, J., Cazenave, F., Gosset, M.: A Comparison of Airborne In Situ Cloud Microphysical Measurement with Ground-Based C-Band Radar Observations in Deep Stratiform Regions of African Squall Lines. J. Appl. Meteor. Climatol. 54, 2461–2477. https://doi.org/10.1175/JAMC-D-14-0262.1, 2015.

Ducrocq, V., Braud, I., Davolio, S., Ferretti, R., Flamant, C., Jansa, A., Kalthoff, N., Richard, E., Taupier-Letage, I., Ayral, P.-A., Belamari, S., Berne, A., Borga, M., Boudevillain, B., Bock, O., Boichard, J.-L., Bouin, M.-N., Bousquet, O., Bouvier, C., Chiggiato, J., Cimini, D., Corsmeier, U., Coppola, L., Cocquerez, P., Defer, E., Delanoë, J., Di Girolamo, P., Doerenbecher, A., Drobinski, P., Dufournet, Y., Fourrié, N., Gourley, J.J., Labatut, L., Lambert, D., Le Coz, J., Marzano, F.S., Molinié, G., Montani, A., Nord, G., Nuret, M., Ramage, K., Rison, W., Roussot, O., Said, F., Schwarzenboeck, A., Testor, P., Van Baelen, J., Vincendon, B., Aran, M., Tamayo, J.: HyMeX-SOP1: The Field Campaign Dedicated to Heavy Precipitation and Flash Flooding in the Northwestern Mediterranean. Bull. Amer. Meteor. Soc. 95, 1083–1100. https://doi.org/10.1175/BAMS-D-12-00244.1, 2013.

Field, P.R., Lawson, R.P., Brown, P.R.A., Lloyd, G., Westbrook, C., Moisseev, D., Miltenberger, A., Nenes, A., Blyth, A., Choularton, T., Connolly, P., Buehl, J., Crosier, J., Cui, Z., Dearden, C., DeMott, P., Flossmann, A., Heymsfield, A., Huang, Y., Kalesse, H., Kanji, Z.A., Korolev, A., Kirchgaessner, A., Lasher-Trapp, S., Leisner, T., McFarquhar, G., Phillips, V., Stith, J., Sullivan, S.: Secondary Ice Production: Current State of the Science and Recommendations for the Future. Meteorological Monographs 58, 7.1-7.20. https://doi.org/10.1175/AMSMONOGRAPHS-D-16-0014.1, 2016.

Field, P.R., Wood, R., Brown, P.R.A., Kaye, P.H., Hirst, E., Greenaway, R., Smith, J.A.: Ice Particle Interarrival Times Measured with a Fast FSSP. J. Atmos. Oceanic Technol. 20, 249–261. https://doi.org/10.1175/1520-0426(2003)020<0249:IPITMW>2.0.CO;2, 2003.

Fiolleau, T., Roca, R.: An Algorithm for the Detection and Tracking of Tropical Mesoscale Convective Systems Using Infrared Images From Geostationary Satellite. Geoscience and Remote Sensing, IEEE Transactions on 51, 4302–4315. https://doi.org/10.1109/TGRS.2012.2227762, 2013.

Fontaine, E., Leroy, D., Schwarzenboeck, A., Delanoë, J., Protat, A., Dezitter, F., Grandin, A., Strapp, J.W., Lilie, L.E.: Evaluation of radar reflectivity factor simulations of ice crystal populations from in situ observations for the retrieval of condensed water content in tropical mesoscale convective systems. Atmos. Meas. Tech. 10, 2239–2252. https://doi.org/10.5194/amt-10-2239-2017, 2017.

Fontaine, E., Schwarzenboeck, A., Delanoë, J., Wobrock, W., Leroy, D., Dupuy, R., Gourbeyre, C., Protat, A.: Constraining mass diameter relations from hydrometeor images and cloud radar reflectivities in tropical continental and oceanic convective anvils. Atmospheric Chemistry and Physics 14, 11367–11392. https://doi.org/10.5194/acp-14-11367-2014, 2014.

Gayet, J.-F., Mioche, G., Bugliaro, L., Protat, A., Minikin, A., Wirth, M., Dörnbrack, A., Shcherbakov, V., Mayer, B., Garnier, A., Gourbeyre, C.: On the observation of unusual high concentration of small chain-like aggregate ice crystals and large ice

https://doi.org/10.5194/acp-2019-502
Preprint. Discussion started: 21 June 2019
© Author(s) 2019. CC BY 4.0 License.

water contents near the top of a deep convective cloud during the CIRCLE-2 experiment. Atmos. Chem. Phys. 12, 727–744. https://doi.org/10.5194/acp-12-727-2012, 2012.

Heymsfield, A.J., Bansemer, A., Heymsfield, G., Fierro, A.O.: Microphysics of Maritime Tropical Convective Updrafts at Temperatures from −20° to −60°. Journal of the Atmospheric Sciences 66, 3530–3562. https://doi.org/10.1175/2009JAS3107.1, 2009.

Heymsfield, A.J., Schmitt, C., Bansemer, A., Twohy, C.H.: Improved Representation of Ice Particle Masses Based on Observations in Natural Clouds. Journal of the Atmospheric Sciences 67, 3303–3318. https://doi.org/10.1175/2010JAS3507.1, 2010.

Heymsfield, A.J., Schmitt, C., Bansemer, A., van Zadelhoff, G.-J., McGill, M.J., Twohy, C., Baumgardner, D.: Effective Radius of Ice Cloud Particle Populations Derived from Aircraft Probes. J. Atmos. Oceanic Technol. 23, 361–380. https://doi.org/10.1175/JTECH1857.1, 2006.

Hogan, R.J., Tian, L., Brown, P.R.A., Westbrook, C.D., Heymsfield, A.J., Eastment, J.D.: Radar Scattering from Ice Aggregates Using the Horizontally Aligned Oblate Spheroid Approximation. J. Appl. Meteor. Climatol. 51, 655–671. https://doi.org/10.1175/JAMC-D-11-074.1, 2011.

Houze, R.A.: Mesoscale convective systems. Reviews of Geophysics 42, n/a–n/a. https://doi.org/10.1029/2004RG000150, 2004.

Huffman, G.J., Bolvin, D.T., Nelkin, E.J., Wolff, D.B., Adler, R.F., Gu, G., Hong, Y., Bowman, K.P., Stocker, E.F.: The TRMM Multisatellite Precipitation Analysis (TMPA): Quasi-Global, Multiyear, Combined-Sensor Precipitation Estimates at Fine Scales. J. Hydrometeor 8, 38–55. https://doi.org/10.1175/JHM560.1, 2007.

Jensen, M.P., Ackerman, T.P., Sekelsky, S.M.: Radiative Impacts of Anvil Cloud during the Maritime Continent Thunderstorm Experiment. J. Appl. Meteor. 41, 473–487. https://doi.org/10.1175/1520-0450(2002)041<0473:RIOACD>2.0.CO;2, 2002.

Jensen, M.P., Del Genio, A.D.: Radiative and Microphysical Characteristics of Deep Convective Systems in the Tropical Western Pacific. Journal of Applied Meteorology 42, 1234–1254. https://doi.org/10.1175/1520-0450(2003)042<1234:RAMCOD>2.0.CO;2, 2003.

Korolev, A., Isaac, G.A.: Shattering during Sampling by OAPs and HVPS. Part I: Snow Particles. J. Atmos. Oceanic Technol. 22, 528–542. https://doi.org/10.1175/JTECH1720.1, 2005.

Korolev, A., Sussman, B.: A Technique for Habit Classification of Cloud Particles. Journal of Atmospheric and Oceanic Technology 17, 1048–1057. https://doi.org/10.1175/1520-0426(2000)017<1048:ATFHCO>2.0.CO;2, 2000.

Lawson, R.P., Jensen, E., Mitchell, D.L., Baker, B., Mo, Q., Pilson, B.: Microphysical and radiative properties of tropical clouds investigated in TC4 and NAMMA. Journal of Geophysical Research: Atmospheres 115, n/a–n/a. https://doi.org/10.1029/2009JD013017, 2010.

Lawson, R.P., O'Connor, D., Zmarzly, P., Weaver, K., Baker, B., Mo, Q., Jonsson, H.: The 2D-S (Stereo) Probe: Design and Preliminary Tests of a New Airborne, High-Speed, High-Resolution Particle Imaging Probe. J. Atmos. Oceanic Technol. 23, 1462–1477. https://doi.org/10.1175/JTECH1927.1, 2006.

Leroy, D., Fontaine, E., Schwarzenboeck, A., Strapp, J.W.: Ice Crystal Sizes in High Ice Water Content Clouds. Part 1: On the computation of Median Mass Diameter from in-situ measurements. Journal of Atmospheric and Oceanic Technology 0, null. https://doi.org/10.1175/JTECH-D-15-0151.1, 2016.

Leroy, D., Fontaine, E., Schwarzenboeck, A., Strapp, J. W., Korolev, A., McFarquhar, G., Dupuy, R., Gourbeyre, C., Lilie, L., Protat, A., Delanoe, J., Dezitter, F. and Grandin, A.: Ice Crystal Sizes in High Ice Water Content Clouds. Part II: Statistics of Mass Diameter Percentiles in Tropical Convection Observed during the HAIC/HIWC Project, Journal of Atmospheric and Oceanic Technology, 34(1), 117–136, doi:10.1175/JTECH-D-15-0246.1, 2017.

Li, J.-L., Jiang, J.H., Waliser, D.E., Tompkins, A.M.: Assessing consistency between EOS MLS and ECMWF analyzed and forecast estimates of cloud ice. Geophysical Research Letters 34, n/a–n/a. https://doi.org/10.1029/2006GL029022, 2007.

© Author(s) 2019. CC BY 4.0 License.

Li, J.-L., Waliser, D.E., Jiang, J.H., Wu, D.L., Read, W., Waters, J.W., Tompkins, A.M., Donner, L.J., Chern, J.-D., Tao, W.-K., Atlas, R., Gu, Y., Liou, K.N., Del Genio, A., Khairoutdinov, M., Gettelman, A.: Comparisons of EOS MLS cloud ice measurements with ECMWF analyses and GCM simulations: Initial results. Geophysical Research Letters 32, n/a–n/a. https://doi.org/10.1029/2005GL023788, 2005.

Locatelli, J.D., Hobbs, P.V.: Fall speeds and masses of solid precipitation particles. Journal of Geophysical Research 79, 2185–2197. https://doi.org/10.1029/JC079i015p02185, 1974.

Madden, R.A., Julian, P.R.: Observations of the 40–50-Day Tropical Oscillation—A Review. Mon. Wea. Rev. 122, 814–837. https://doi.org/10.1175/1520-0493(1994)122<0814:OOTDTO>2.0.CO;2, 1994.

Madden, R.A., Julian, P.R.: Detection of a 40–50 Day Oscillation in the Zonal Wind in the Tropical Pacific. J. Atmos. Sci. 28, 702–708. https://doi.org/10.1175/1520-0469(1971)028<0702:DOADOI>2.0.CO;2, 1971.

Magono, C., Lee, C., Woo.: Meteorological Classification of Natural Snow Crystals. Journal of the Faculty of Science, Hokkaido University 2(4): 321-335, 1966.

Martini, A., Viltard, N., Ellis, S.M., Fontaine, E.: Ice microphysics retrieval in the convective systems of the Indian Ocean during the CINDY–DYNAMO campaign. Atmospheric Research. http://dx.doi.org/10.1016/j.atmosres.2014.12.013, 2015.

Mitchell, D.L.: Use of Mass- and Area-Dimensional Power Laws for Determining Precipitation Particle Terminal Velocities. J. Atmos. Sci. 53, 1710–1723. https://doi.org/10.1175/1520-0469(1996)053<1710:UOMAAD>2.0.CO;2, 1996.

Phillips, V.T.J., Patade, S., Gutierrez, J., Bansemer,: A. Secondary ice production by fragmentation of freezing drops: formulation and theory. J. Atmos. Sci. https://doi.org/10.1175/JAS-D-17-0190.1, 2018.

Protat, A., Zawadzki, I.: A Variational Method for Real-Time Retrieval of Three-Dimensional Wind Field from Multiple-Doppler Bistatic Radar Network Data. J. Atmos. Oceanic Technol. 16, 432–449. https://doi.org/10.1175/1520-0426(1999)016<0432:AVMFRT>2.0.CO;2, 1999.

Protat, A., Bouniol, D., Delanoë, J., O'Connor, E., May, P.T., Plana-Fattori, A., Hasson, A., Görsdorf, U., Heymsfield, A.J.: Assessment of Cloudsat Reflectivity Measurements and Ice Cloud Properties Using Ground-Based and Airborne Cloud Radar Observations. J. Atmos. Oceanic Technol. 26, 1717–1741. https://doi.org/10.1175/2009JTECHA1246.1, 2009.

Protat, A., Delanoë, J., Strapp, J.W., Fontaine, E., Leroy, D., Schwarzenboeck, A., Lilie, L., Davison, C., Dezitter, F., Grandin, A., Weber, M.: The Measured Relationship between Ice Water Content and Cloud Radar Reflectivity in Tropical Convective Clouds. Journal of Applied Meteorology and Climatology 55, 1707–1729. https://doi.org/10.1175/JAMC-D-15-0248.1

Pruppacher, H.R., Klett, J.D., Wang, P.K., 1998. Microphysics of Clouds and Precipitation. Aerosol Science and Technology 28, 381–382. https://doi.org/10.1080/02786829808965531, 2016.

Roca, R., Brogniez, H., Chambon, P., Chomette, O., Cloché, S., Gosset, M.E., Mahfouf, J., Raberanto, P., Viltard, N.: The Megha-Tropiques mission: a review after three years in orbit. Frontiers in Earth Science 3. https://doi.org/10.3389/feart.2015.00017, 2015.

Schmitt, C.G., Heymsfield, A.J.: The Dimensional Characteristics of Ice Crystal Aggregates from Fractal Geometry. Journal of the Atmospheric Sciences 67, 1605–1616. https://doi.org/10.1175/2009JAS3187.1, 2010.

Smith, W.L.: 4-D Cloud Properties from Passive Satellite Data and Applications to Resolve the Flight Icing Threat to Aircraft. University Of Wisconsin-Madison. Ph.D thesis, 179pp., 2014.

Stephens, G.L., Vane, D.G., Boain, R.J., Mace, G.G., Sassen, K., Wang, Z., Illingworth, A.J., O'Connor, E.J., Rossow, W.B., Durden, S.L., Miller, S.D., Austin, R.T., Benedetti, A., Mitrescu, C., CloudSat Science Team, T.: THE CLOUDSAT MISSION AND THE A-TRAIN. Bull. Amer. Meteor. Soc. 83, 1771–1790. https://doi.org/10.1175/BAMS-83-12-1771, 2002.

Stith, J.L., Avallone, L.M., Bansemer, A., Basarab, B., Dorsi, S.W., Fuchs, B., Lawson, R.P., Rogers, D.C., Rutledge, S., Toohey, D.W.: Ice particles in the upper anvil regions of midlatitude continental thunderstorms: the case for frozen-drop aggregates. Atmospheric Chemistry and Physics 14, 1973–1985. https://doi.org/10.5194/acp-14-1973-2014, 2014.

https://doi.org/10.5194/acp-2019-502
Preprint. Discussion started: 21 June 2019
© Author(s) 2019. CC BY 4.0 License.

Atmospheric Chemistry and Physics Discussions

Strapp, J.W., Lilie, L.E., Ratvasky, T.P., Davison, C.R., and C. Dumont.: Isokinetic TWC Evaporator Probe: Development of the IKP2 and Performance Testing for the HAIC-HIWC Darwin 2014 and Cayenne Field Campaigns, 8th AIAA Atmospheric and Space Environments Conference, AIAA Aviation, AIAA 2016-4059. http://dx.doi.org/10.2514/6.2016-4059, 2016a.

Strapp, J. W., G. A. Isaac. A. Korolev, T. Ratvasky, R. Potts, P. May, A. Protat, P. Minnis, A. Ackerman, A. Fridlind, J. Haggerty, and J. Riley.: The High Ice Water Content (HIWC) Study of deep convective clouds: Science and technical plan. FAA Rep. DOT/FAA/TC-14/31, available at http://www.tc.faa.gov/its/worldpac/techrpt/tc14-31.pdf. 105 pp., 2016b

Yano, J.-I., Phillips, V.T.J.: Ice–Ice Collisions: An Ice Multiplication Process in Atmospheric Clouds. J. Atmos. Sci. 68, 322–333. https://doi.org/10.1175/2010JAS3607.1, 2011.

Van de Hulst, H.C.: Light scattering by small particles, 470 pp, Dover, Mineola, N.Y., 1981.

Yost, C.R., Bedka, K.M., Minnis, P., Nguyen, L., Strapp, J.W., Palikonda, R., Khlopenkov, K., Spangenberg, D., Smith Jr., W.L., Protat, A., Delanoe, J.: A prototype method for diagnosing high ice water content probability using satellite imager data. Atmos. Meas. Tech. 11, 1615–1637. https://doi.org/10.5194/amt-11-1615-2018, 2018.

Yost, C.R., Minnis, P., Ayers, J.K., Spangenberg, D.A., Heymsfield, A.J., Bansemer, A., McGill, M.J., Hlavka, D.L.: Comparison of GOES-retrieved and in situ measurements of deep convective anvil cloud microphysical properties during the Tropical Composition, Cloud and Climate Coupling Experiment (TC4). Journal of Geophysical Research: Atmospheres 115, n/a–n/a. https://doi.org/10.1029/2009JD013313, 2010.

Appendices A: Tables.

Table A 1: Percentile of Radar reflectivity factors (Z) in [dBZ], shown in solid line in Figure 1.

T [K]	1^{rst} [dBZ]	10th [dBZ]	30th [dBZ]	50th [dBZ]	70th [dBZ]	90th [dBZ]	99th [dBZ]
172,5	-7,00	-3,45	-0,96	0,90	2,83	5,32	11,70
177,5	-8,33	-5,14	-1,96	0,43	2,81	5,49	8,69
182,5	-9,44	-5,96	-3,01	-0,56	2,39	5,51	8,92
187,5	-9,93	-6,66	-4,07	-1,67	1,08	5,33	8,53
192,5	-10,15	-6,79	-4,14	-1,85	0,63	4,97	8,78
197,5	-11,08	-6,95	-3,80	-1,06	1,48	5,18	9,24
202,5	-12,08	-7,53	-3,87	-0,74	2,13	5,37	9,82
207,5	-13,25	-8,06	-4,00	-0,53	2,69	5,75	10,22
212,5	-16,88	-8,65	-4,11	-0,44	3,05	6,28	10,66
217,5	-26,79	-10,67	-4,54	-0,44	3,37	6,93	11,27
222,5	-30,13	-12,58	-5,21	-0,30	3,88	7,71	12,01
227,5	-28,30	-13,55	-5,17	0,06	4,61	8,60	12,94
232,5	-26,65	-13,08	-4,49	0,75	5,54	9,70	14,15
237,5	-26,54	-11,80	-3,26	2,11	6,76	10,92	15,08
242,5	-24,53	-10,27	-1,76	3,62	7,96	11,76	15,76
247,5	-23,78	-8,58	-0,20	5,16	9,13	12,51	15,98
252,5	-22,15	-6,76	1,64	6,58	10,14	13,17	16,37
257,5	-22,05	-5,97	3,18	7,89	11,09	13,78	16,86
262,5	-21,30	-5,83	4,01	8,59	11,44	14,11	17,43
267,5	-21,90	-5,65	3,89	8,26	11,03	13,72	17,34
272,5	-20,68	-5,77	2,88	6,86	9,57	12,60	16,66
277,5	-17,52	-4,84	2,73	6,25	8,90	12,07	16,42
282,5	-15,52	-6,62	-1,12	2,30	5,03	8,33	15,06
287,5	-14,40	-7,55	-2,90	0,40	3,18	7,88	38,13

https://doi.org/10.5194/acp-2019-502
Preprint. Discussion started: 21 June 2019
© Author(s) 2019. CC BY 4.0 License.

Atmospheric Chemistry and Physics Discussions

292,5	-13,67	-7,94	-4,07	-1,37	1,04	4,55	10,49
297,5	-12,95	-7,52	-4,00	-1,18	2,90	27,11	42,87
302,5	-10,98	-4,72	0,81	8,39	14,21	29,74	44,98

Table A 2: Ice water content (IWC) in [g m^{-3}] (Figure 5-a)

MCS RZ		T [215;225[	T ∈ [225;235[	T∈ [235,245[	T∈ [245;255[	T∈ [255;265[	T ∈ [265;273,15[
	25th	0,016	0,017	0,016	0,016	0,016	0,016
2	**50th**	**0,024**	**0,024**	**0,025**	**0,023**	**0,025**	**0,026**
	75th	0,029	0,034	0,042	0,033	0,041	0,063
	25th	0,042	0,032	0,031	0,040	0,043	0,052
3	**50th**	**0,053**	**0,052**	**0,054**	**0,062**	**0,070**	**0,098**
	75th	0,062	0,076	0,084	0,093	0,111	0,148
	25th	0,081	0,082	0,090	0,112	0,149	0,136
4	**50th**	**0,110**	**0,119**	**0,130**	**0,160**	**0,212**	**0,198**
	75th	0,138	0,163	0,180	0,216	0,298	0,284
	25th	0,176	0,199	0,221	0,272	0,316	0,246
5	**50th**	**0,220**	**0,261**	**0,295**	**0,351**	**0,413**	**0,342**
	75th	0,276	0,340	0,395	0,454	0,508	0,476
	25th	0,402	0,430	0,476	0,561	0,556	0,479
6	**50th**	**0,538**	**0,572**	**0,628**	**0,690**	**0,701**	**0,624**
	75th	0,662	0,742	0,822	0,818	0,863	0,762
	25th	0,869	0,767	0,994	1,057	1,102	0,928
7	**50th**	**1,083**	**1,069**	**1,294**	**1,295**	**1,402**	**1,204**
	75th	1,365	1,424	1,640	1,704	1,797	1,526
	25th	1,604	1,644	1,951	2,116	2,009	1,443
8	**50th**	**1,810**	**2,051**	**2,306**	**2,515**	**2,268**	**1,827**
	75th	1,998	2,352	2,690	2,907	2,555	2,282

5

Table A 3: visible extinction (σ) in [m^{-1}] (Figure 6-a).

MCS RZ		T ∈[215;225[	T∈ [225;235[	T∈ [235,245[	T ∈ [245;255[	T∈ [255;265[	T [265;273,15[
	25th	0,00047	0,00071	0,00044	0,00045	0,00031	0,00013
2	**50th**	**0,00097**	**0,00112**	**0,00102**	**0,00088**	**0,00078**	**0,00060**
	75th	0,00125	0,00172	0,00169	0,00128	0,00184	0,00413
	25th	0,00253	0,00188	0,00166	0,00140	0,00135	0,00118
3	**50th**	**0,00321**	**0,00262**	**0,00225**	**0,00205**	**0,00226**	**0,00217**
	75th	0,00363	0,00352	0,00316	0,00310	0,00337	0,00453
	25th	0,00521	0,00400	0,00342	0,00355	0,00400	0,00284
4	**50th**	**0,00616**	**0,00529**	**0,00466**	**0,00500**	**0,00542**	**0,00410**
	75th	0,00803	0,00697	0,00640	0,00685	0,00769	0,00762
	25th	0,00978	0,00855	0,00785	0,00765	0,00749	0,00457
5	**50th**	**0,01237**	**0,01101**	**0,01042**	**0,01030**	**0,00997**	**0,00693**
	75th	0,01484	0,01413	0,01348	0,01292	0,01281	0,01223

https://doi.org/10.5194/acp-2019-502
Preprint. Discussion started: 21 June 2019
© Author(s) 2019. CC BY 4.0 License.

Atmospheric Chemistry and Physics Discussions

	25th	0,01972	0,01674	0,01550	0,01512	0,01169	0,00900
6	**50th**	**0,02478**	**0,02256**	**0,02088**	**0,01969**	**0,01596**	**0,01173**
	75th	0,03040	0,02904	0,02745	0,02387	0,01995	0,01515
	25th	0,03969	0,02892	0,03133	0,02726	0,02393	0,01722
7	**50th**	**0,04893**	**0,04083**	**0,04149**	**0,03386**	**0,03103**	**0,02404**
	75th	0,06096	0,05435	0,05773	0,04571	0,04127	0,03271
	25th	0,06965	0,05976	0,05243	0,05033	0,04139	0,01991
8	**50th**	**0,07865**	**0,07116**	**0,06944**	**0,06461**	**0,05125**	**0,03443**
	75th	0,08871	0,08247	0,08206	0,07942	0,06088	0,04287

Table A 4: Total concentration beyond 15µm (N_T) in [L^{-1}] (Figure 8-a).

MCS RZ		T ∈[215;225[	T∈ [225;235[	T∈ [235,245[	T∈ [245;255[	T∈ [255;265[	T [265;273,15[
	25th	3,65E+01	7,73E+01	3,12E+01	2,51E+01	1,25E+01	6,01E+00
2	**50th**	**7,41E+01**	**1,53E+02**	**8,32E+01**	**5,03E+01**	**3,11E+01**	**4,26E+01**
	75th	1,58E+02	3,62E+02	1,73E+02	1,20E+02	6,54E+02	2,14E+03
	25th	1,67E+02	1,11E+02	5,11E+01	3,99E+01	3,24E+01	3,58E+01
3	**50th**	**1,91E+02**	**1,92E+02**	**8,26E+01**	**7,46E+01**	**5,95E+01**	**7,92E+01**
	75th	3,79E+02	4,22E+02	1,42E+02	1,36E+02	1,10E+02	7,41E+02
	25th	2,20E+02	1,56E+02	7,86E+01	6,92E+01	7,37E+01	6,47E+01
4	**50th**	**4,65E+02**	**2,42E+02**	**1,34E+02**	**1,22E+02**	**1,23E+02**	**1,06E+02**
	75th	7,04E+02	5,41E+02	2,33E+02	2,27E+02	2,22E+02	4,02E+02
	25th	6,63E+02	3,07E+02	1,70E+02	1,44E+02	1,19E+02	8,88E+01
5	**50th**	**9,67E+02**	**5,45E+02**	**2,72E+02**	**2,10E+02**	**1,87E+02**	**2,14E+02**
	75th	1,17E+03	9,25E+02	4,39E+02	3,14E+02	3,11E+02	1,37E+03
	25th	1,13E+03	5,70E+02	3,32E+02	2,73E+02	1,71E+02	1,38E+02
6	**50th**	**1,40E+03**	**9,66E+02**	**5,64E+02**	**4,74E+02**	**2,51E+02**	**2,15E+02**
	75th	2,10E+03	1,77E+03	9,09E+02	7,59E+02	3,93E+02	6,93E+02
	25th	2,28E+03	9,57E+02	7,26E+02	6,30E+02	3,37E+02	2,70E+02
7	**50th**	**3,40E+03**	**1,91E+03**	**1,35E+03**	**9,98E+02**	**5,37E+02**	**5,58E+02**
	75th	5,05E+03	3,35E+03	2,45E+03	1,53E+03	8,78E+02	1,10E+03
	25th	6,26E+03	3,08E+03	7,64E+02	7,81E+02	7,63E+02	4,61E+02
8	**50th**	**9,55E+03**	**5,13E+03**	**1,68E+03**	**1,96E+03**	**1,13E+03**	**8,05E+02**
	75th	1,28E+04	7,37E+03	6,09E+03	5,20E+03	1,82E+03	1,99E+03

5

Table A 5: Total concentration since 50µm ($N_{T\,50}$) in [L^{-1}] (Figure 9-a).

MCS RZ		T ∈[215;225[	T∈ [225;235[	T∈ [235,245[	T∈ [245;255[	T∈ [255;265[	T [265;273,15[
	25th	8,65E+00	1,72E+01	5,24E+00	3,98E+00	1,18E+00	7,57E-01
2	**50th**	**2,13E+01**	**3,21E+01**	**1,68E+01**	**9,13E+00**	**4,49E+00**	**3,32E+00**
	75th	3,99E+01	5,77E+01	3,26E+01	1,90E+01	1,21E+01	4,28E+01
	25th	4,16E+01	3,05E+01	1,35E+01	8,50E+00	4,42E+00	2,18E+00
3	**50th**	**4,75E+01**	**4,70E+01**	**2,19E+01**	**1,39E+01**	**8,82E+00**	**4,79E+00**
	75th	8,35E+01	7,79E+01	3,68E+01	2,60E+01	1,74E+01	2,07E+01

https://doi.org/10.5194/acp-2019-502
Preprint. Discussion started: 21 June 2019
© Author(s) 2019. CC BY 4.0 License.

Atmospheric Chemistry and Physics Discussions

	25th	6,38E+01	4,66E+01	2,15E+01	1,47E+01	1,02E+01	7,28E+00
4	**50th**	**1,05E+02**	**7,25E+01**	**3,56E+01**	**2,78E+01**	**1,72E+01**	**1,38E+01**
	75th	1,64E+02	1,23E+02	6,21E+01	4,49E+01	3,03E+01	2,46E+01
	25th	1,57E+02	9,14E+01	4,70E+01	3,33E+01	1,83E+01	1,11E+01
5	**50th**	**2,06E+02**	**1,39E+02**	**7,26E+01**	**5,66E+01**	**3,03E+01**	**2,30E+01**
	75th	2,49E+02	2,10E+02	1,14E+02	8,17E+01	4,78E+01	4,39E+01
	25th	2,68E+02	1,55E+02	9,50E+01	7,22E+01	3,00E+01	1,78E+01
6	**50th**	**3,28E+02**	**2,47E+02**	**1,50E+02**	**1,06E+02**	**4,91E+01**	**2,86E+01**
	75th	4,84E+02	4,12E+02	2,34E+02	1,45E+02	7,25E+01	6,47E+01
	25th	5,65E+02	2,49E+02	2,07E+02	1,36E+02	7,20E+01	3,35E+01
7	**50th**	**7,83E+02**	**4,92E+02**	**3,41E+02**	**1,90E+02**	**1,13E+02**	**9,02E+01**
	75th	1,12E+03	8,00E+02	6,20E+02	3,08E+02	1,84E+02	1,74E+02
	25th	1,34E+03	7,26E+02	2,06E+02	1,90E+02	1,82E+02	7,29E+01
8	**50th**	**1,82E+03**	**1,09E+03**	**3,86E+02**	**4,01E+02**	**2,83E+02**	**1,57E+02**
	75th	2,30E+03	1,51E+03	1,31E+03	9,29E+02	4,95E+02	3,10E+02

Table A 6: Total concentration since 500µm ($N_{T\,500}$) in [L^{-1}] (Figure 10-a).

MCS RZ		T ∈[215;225[	T∈ [225;235[	T∈ [235,245[	T∈ [245;255[	T∈ [255;265[	T∈ [265;273,15[
	25th	0,00E+00	1,96E-02	4,08E-02	1,33E-01	8,31E-02	1,68E-02
2	**50th**	**5,20E-02**	**7,23E-02**	**1,73E-01**	**3,41E-01**	**2,86E-01**	**8,60E-02**
	75th	2,05E-01	1,88E-01	4,13E-01	7,27E-01	6,52E-01	3,37E-01
	25th	1,12E+00	4,23E-01	8,37E-01	1,09E+00	8,64E-01	3,57E-01
3	**50th**	**1,57E+00**	**8,68E-01**	**1,33E+00**	**1,61E+00**	**1,40E+00**	**6,67E-01**
	75th	2,03E+00	1,43E+00	1,91E+00	2,22E+00	2,07E+00	1,29E+00
	25th	2,77E+00	1,92E+00	2,26E+00	2,96E+00	2,73E+00	1,67E+00
4	**50th**	**3,77E+00**	**2,73E+00**	**3,15E+00**	**3,95E+00**	**3,91E+00**	**2,40E+00**
	75th	4,54E+00	3,84E+00	4,40E+00	5,06E+00	5,51E+00	3,52E+00
	25th	5,61E+00	5,55E+00	5,71E+00	5,83E+00	5,29E+00	2,82E+00
5	**50th**	**7,78E+00**	**7,26E+00**	**7,68E+00**	**7,78E+00**	**7,19E+00**	**4,15E+00**
	75th	9,34E+00	9,48E+00	1,01E+01	1,02E+01	8,98E+00	6,60E+00
	25th	1,25E+01	1,27E+01	1,19E+01	1,21E+01	9,61E+00	3,83E+00
6	**50th**	**1,55E+01**	**1,60E+01**	**1,56E+01**	**1,45E+01**	**1,24E+01**	**6,07E+00**
	75th	1,97E+01	2,02E+01	2,06E+01	1,74E+01	1,53E+01	9,17E+00
	25th	2,26E+01	2,00E+01	2,41E+01	2,01E+01	1,83E+01	8,29E+00
7	**50th**	**2,83E+01**	**2,65E+01**	**3,08E+01**	**2,52E+01**	**2,42E+01**	**1,54E+01**
	75th	3,34E+01	3,35E+01	3,96E+01	3,44E+01	3,35E+01	2,40E+01
	25th	1,95E+01	2,69E+01	3,35E+01	3,71E+01	2,67E+01	1,06E+01
8	**50th**	**2,38E+01**	**3,75E+01**	**4,89E+01**	**4,99E+01**	**3,73E+01**	**2,43E+01**
	75th	2,85E+01	5,23E+01	7,29E+01	6,87E+01	4,86E+01	3,80E+01

Table A 7: pre-factor α of mass size relationship in [g $cm^{-\beta}$] (Figure 12-a).

MCS RZ		T ∈[215;225[	T∈ [225;235[	T∈ [235,245[	T∈ [245;255[	T∈ [255;265[	T [265;273,15[
2	25th	0,00095	0,00042	0,00053	0,00086	0,00152	0,00114

https://doi.org/10.5194/acp-2019-502
Preprint. Discussion started: 21 June 2019
© Author(s) 2019. CC BY 4.0 License.

Atmospheric Chemistry and Physics Discussions

	50th	**0,00269**	**0,00099**	**0,00128**	**0,00172**	**0,00341**	**0,00322**
	75th	0,00574	0,00276	0,00320	0,00312	0,00876	0,00809
	25th	0,00092	0,00059	0,00099	0,00149	0,00190	0,00319
3	**50th**	**0,00126**	**0,00115**	**0,00181**	**0,00241**	**0,00341**	**0,00687**
	75th	0,00154	0,00197	0,00299	0,00379	0,00630	0,01077
	25th	0,00142	0,00126	0,00184	0,00250	0,00343	0,00385
4	**50th**	**0,00180**	**0,00198**	**0,00274**	**0,00340**	**0,00505**	**0,00592**
	75th	0,00235	0,00282	0,00404	0,00470	0,00711	0,00826
	25th	0,00195	0,00188	0,00267	0,00333	0,00422	0,00481
5	**50th**	**0,00241**	**0,00258**	**0,00351**	**0,00414**	**0,00562**	**0,00658**
	75th	0,00300	0,00336	0,00455	0,00529	0,00742	0,00950
	25th	0,00189	0,00210	0,00324	0,00419	0,00486	0,00595
6	**50th**	**0,00271**	**0,00285**	**0,00403**	**0,00513**	**0,00625**	**0,00782**
	75th	0,00334	0,00380	0,00492	0,00638	0,00793	0,01014
	25th	0,00163	0,00253	0,00325	0,00466	0,00527	0,00594
7	**50th**	**0,00245**	**0,00351**	**0,00415**	**0,00560**	**0,00637**	**0,00774**
	75th	0,00326	0,00447	0,00517	0,00668	0,00776	0,01077
	25th	0,00214	0,00302	0,00363	0,00405	0,00538	0,00637
8	**50th**	**0,00418**	**0,00485**	**0,00496**	**0,00558**	**0,00712**	**0,00953**
	75th	0,00748	0,00750	0,00679	0,00819	0,01173	0,01886

Table A 8: exponent of mass-size relationship β [no dimension] (Figure 11-a).

MCS RZ		T ∈[215;225[	T∈ [225;235[	T∈ [235,245[	T∈ [245;255[	T∈ [255;265[	T [265;273,15[
	25th	1,67	1,54	1,58	1,66	1,74	1,66
2	**50th**	**1,86**	**1,76**	**1,78**	**1,85**	**1,95**	**1,93**
	75th	2,07	1,96	1,99	2,02	2,21	2,08
	25th	1,80	1,65	1,75	1,79	1,86	1,86
3	**50th**	**1,88**	**1,82**	**1,91**	**1,92**	**2,00**	**2,08**
	75th	1,95	1,96	2,04	2,05	2,17	2,35
	25th	1,90	1,82	1,87	1,91	1,96	1,94
4	**50th**	**1,98**	**1,94**	**1,99**	**2,02**	**2,10**	**2,10**
	75th	2,03	2,04	2,10	2,12	2,22	2,26
	25th	1,99	1,91	1,96	1,97	2,02	2,05
5	**50th**	**2,07**	**2,00**	**2,06**	**2,05**	**2,11**	**2,16**
	75th	2,12	2,08	2,14	2,14	2,21	2,29
	25th	1,91	1,92	2,01	2,04	2,03	2,04
6	**50th**	**2,06**	**2,01**	**2,09**	**2,11**	**2,11**	**2,16**
	75th	2,14	2,11	2,16	2,19	2,20	2,26
	25th	1,86	1,97	1,99	2,06	2,06	2,07
7	**50th**	**2,00**	**2,08**	**2,08**	**2,13**	**2,13**	**2,15**
	75th	2,10	2,17	2,16	2,19	2,19	2,26
	25th	1,93	1,98	1,97	2,01	2,07	2,10
8	**50th**	**2,11**	**2,13**	**2,08**	**2,13**	**2,16**	**2,21**
	75th	2,27	2,25	2,19	2,22	2,29	2,34

https://doi.org/10.5194/acp-2019-502
Preprint. Discussion started: 21 June 2019
© Author(s) 2019. CC BY 4.0 License.

Atmospheric Chemistry and Physics Discussions

Table A 9: *max(D_{max})* in [cm] (Figure 13-a).

MCS RZ		T ∈[215;225[	T∈ [225;235[	T∈ [235,245[	T∈ [245;255[	T∈ [255;265[	T [265;273,15[
2	25th	0,048	0,061	0,090	0,105	0,125	0,105
	50th	**0,090**	**0,095**	**0,110**	**0,140**	**0,195**	**0,165**
	75th	0,120	0,115	0,140	0,195	0,361	0,255
3	25th	0,155	0,120	0,145	0,155	0,205	0,245
	50th	**0,175**	**0,145**	**0,190**	**0,205**	**0,310**	**0,435**
	75th	0,195	0,180	0,265	0,295	0,620	0,762
4	25th	0,205	0,170	0,195	0,215	0,280	0,332
	50th	**0,235**	**0,212**	**0,260**	**0,347**	**0,525**	**0,445**
	75th	0,265	0,270	0,380	0,615	0,790	0,775
5	25th	0,235	0,225	0,265	0,280	0,350	0,415
	50th	**0,280**	**0,280**	**0,375**	**0,405**	**0,625**	**0,615**
	75th	0,340	0,355	0,575	0,685	0,820	0,795
6	25th	0,245	0,245	0,310	0,335	0,385	0,475
	50th	**0,315**	**0,310**	**0,460**	**0,665**	**0,625**	**0,735**
	75th	0,395	0,435	0,680	0,880	0,810	0,838
7	25th	0,225	0,270	0,325	0,445	0,480	0,557
	50th	**0,285**	**0,397**	**0,452**	**0,675**	**0,675**	**0,745**
	75th	0,375	0,595	0,645	0,846	0,810	0,825
8	25th	0,335	0,315	0,395	0,445	0,445	0,455
	50th	**0,455**	**0,480**	**0,555**	**0,632**	**0,595**	**0,635**
	75th	0,665	0,730	0,790	0,825	0,740	0,745

Table A 10: Second Moment of PSD (M_2) [m^{-1}] (Figure 14-a).

MCS RZ		T∈ [215;225[	T∈ [225;235[	T∈ [235,245[	T∈ [245;255[	T∈ [255;265[	T ∈ [265;273,15[
2	25th	4,33E-04	5,99E-04	3,90E-04	4,41E-04	3,03E-04	1,22E-04
	50th	**8,04E-04**	**9,32E-04**	**8,67E-04**	**8,18E-04**	**7,10E-04**	**5,50E-04**
	75th	9,78E-04	1,37E-03	1,42E-03	1,20E-03	1,57E-03	2,62E-03
3	25th	2,26E-03	1,71E-03	1,50E-03	1,36E-03	1,26E-03	1,01E-03
	50th	**2,85E-03**	**2,32E-03**	**2,03E-03**	**1,98E-03**	**2,07E-03**	**1,83E-03**
	75th	3,21E-03	3,08E-03	2,80E-03	2,80E-03	3,01E-03	3,50E-03
4	25th	4,59E-03	3,60E-03	3,10E-03	3,30E-03	3,70E-03	2,71E-03
	50th	**5,43E-03**	**4,73E-03**	**4,17E-03**	**4,60E-03**	**4,99E-03**	**3,72E-03**
	75th	6,99E-03	6,10E-03	5,69E-03	6,38E-03	6,91E-03	6,39E-03
5	25th	8,78E-03	7,82E-03	7,20E-03	7,11E-03	7,07E-03	4,43E-03
	50th	**1,13E-02**	**9,99E-03**	**9,56E-03**	**9,55E-03**	**9,19E-03**	**6,49E-03**
	75th	1,34E-02	1,27E-02	1,23E-02	1,21E-02	1,17E-02	1,07E-02
6	25th	1,79E-02	1,60E-02	1,42E-02	1,40E-02	1,10E-02	8,29E-03
	50th	**2,28E-02**	**2,09E-02**	**1,95E-02**	**1,83E-02**	**1,48E-02**	**1,06E-02**
	75th	2,77E-02	2,66E-02	2,53E-02	2,25E-02	1,85E-02	1,38E-02
7	25th	3,57E-02	2,75E-02	2,93E-02	2,57E-02	2,27E-02	1,53E-02
	50th	**4,41E-02**	**3,79E-02**	**3,86E-02**	**3,22E-02**	**2,96E-02**	**2,21E-02**
	75th	5,39E-02	4,94E-02	5,29E-02	4,31E-02	3,95E-02	3,11E-02

https://doi.org/10.5194/acp-2019-502
Preprint. Discussion started: 21 June 2019
© Author(s) 2019. CC BY 4.0 License.

Atmospheric Chemistry and Physics Discussions

	25th	6,02E-02	5,30E-02	4,92E-02	4,77E-02	3,96E-02	1,85E-02
8	**50th**	**6,73E-02**	**6,39E-02**	**6,39E-02**	**6,21E-02**	**4,95E-02**	**3,23E-02**
	75th	7,41E-02	7,30E-02	7,36E-02	7,53E-02	5,84E-02	4,27E-02

Table A 11: Third moment of PSD (M_3) in [1] (Figure 15-a).

MCS RZ		T ∈[215;225[	T∈ [225;235[	T∈ [235,245[	T∈ [245;255[	T∈ [255;265[	T ∈ [265;273,15[
	25th	1,29E-07	1,30E-07	1,07E-07	1,43E-07	1,68E-07	5,16E-08
2	**50th**	**1,78E-07**	**2,09E-07**	**2,29E-07**	**2,98E-07**	**3,83E-07**	**1,92E-07**
	75th	2,12E-07	2,98E-07	4,00E-07	5,38E-07	6,36E-07	5,66E-07
	25th	7,85E-07	5,40E-07	6,75E-07	7,36E-07	8,89E-07	7,74E-07
3	**50th**	**1,06E-06**	**8,08E-07**	**9,69E-07**	**1,11E-06**	**1,56E-06**	**1,92E-06**
	75th	1,27E-06	1,08E-06	1,43E-06	1,67E-06	3,59E-06	5,23E-06
	25th	1,85E-06	1,47E-06	1,75E-06	2,15E-06	3,08E-06	2,52E-06
4	**50th**	**2,44E-06**	**1,99E-06**	**2,43E-06**	**3,57E-06**	**5,71E-06**	**3,98E-06**
	75th	3,08E-06	2,80E-06	3,61E-06	5,99E-06	1,13E-05	1,12E-05
	25th	4,13E-06	3,92E-06	4,59E-06	4,80E-06	5,95E-06	5,13E-06
5	**50th**	**5,55E-06**	**5,20E-06**	**6,64E-06**	**7,83E-06**	**1,08E-05**	**8,69E-06**
	75th	7,08E-06	6,84E-06	9,57E-06	1,13E-05	1,93E-05	1,93E-05
	25th	9,42E-06	8,92E-06	9,88E-06	9,93E-06	9,93E-06	8,90E-06
6	**50th**	**1,19E-05**	**1,17E-05**	**1,45E-05**	**1,77E-05**	**1,66E-05**	**1,75E-05**
	75th	1,43E-05	1,51E-05	1,93E-05	2,50E-05	2,54E-05	2,62E-05
	25th	1,66E-05	1,75E-05	1,98E-05	2,51E-05	2,37E-05	1,91E-05
7	**50th**	**2,02E-05**	**2,16E-05**	**2,63E-05**	**3,05E-05**	**3,35E-05**	**3,28E-05**
	75th	2,36E-05	2,71E-05	3,20E-05	3,82E-05	4,24E-05	4,25E-05
	25th	2,07E-05	2,20E-05	2,80E-05	3,13E-05	2,74E-05	1,54E-05
8	**50th**	**2,27E-05**	**2,69E-05**	**3,29E-05**	**4,16E-05**	**3,89E-05**	**2,84E-05**
	75th	2,45E-05	3,21E-05	4,30E-05	5,76E-05	5,22E-05	4,57E-05

Table A 12: coefficient *A* in [kg m^{-2}] (Figure 16-a).

MCS RZ		T ∈[215;225[	T∈ [225;235[	T∈ [235,245[	T∈ [245;255[	T∈ [255;265[	T ∈ [265;273,15[
	25th	0,021	0,018	0,018	0,019	0,017	0,019
2	**50th**	**0,031**	**0,025**	**0,032**	**0,031**	**0,041**	**0,048**
	75th	0,042	0,038	0,064	0,054	0,085	0,163
	25th	0,017	0,016	0,018	0,024	0,025	0,029
3	**50th**	**0,018**	**0,023**	**0,026**	**0,032**	**0,037**	**0,052**
	75th	0,020	0,030	0,036	0,041	0,051	0,071
	25th	0,017	0,019	0,023	0,027	0,034	0,037
4	**50th**	**0,020**	**0,025**	**0,029**	**0,034**	**0,042**	**0,048**
	75th	0,021	0,031	0,038	0,043	0,051	0,061
	25th	0,018	0,022	0,026	0,031	0,038	0,038
5	**50th**	**0,020**	**0,026**	**0,031**	**0,037**	**0,045**	**0,047**
	75th	0,023	0,030	0,037	0,045	0,053	0,061

https://doi.org/10.5194/acp-2019-502
Preprint. Discussion started: 21 June 2019
© Author(s) 2019. CC BY 4.0 License.

Atmospheric Chemistry and Physics Discussions

	25th	0,021	0,024	0,028	0,033	0,042	0,047
6	**50th**	**0,023**	**0,027**	**0,032**	**0,037**	**0,048**	**0,057**
	75th	0,026	0,031	0,038	0,045	0,057	0,069
	25th	0,023	0,025	0,028	0,036	0,041	0,047
7	**50th**	**0,024**	**0,028**	**0,032**	**0,040**	**0,046**	**0,054**
	75th	0,027	0,031	0,038	0,044	0,053	0,064
	25th	0,025	0,029	0,032	0,035	0,041	0,048
8	**50th**	**0,027**	**0,032**	**0,038**	**0,039**	**0,045**	**0,060**
	75th	0,030	0,035	0,045	0,047	0,053	0,080

5